International Journal of Earth Sciences
https://doi.org/10.1007/s00531-025-02511-4

ORIGINAL PAPER

Decoding multiple ore mineral remobilization processes during polyphase deformational phases from the Precambrian Pyhäsalmi VMS deposit halo, Central Finland: new insights from mineralogy, mineral chemistry and micro-CT

Sk Rakibul Islam[1] · Esa Heilimo[1] · Jukka Kuva[2] · Ermei Mäkilä[3] · Timo Mäki[4]

Received: 18 December 2024 / Accepted: 1 May 2025

Abstract

The Precambrian bimodal Pyhäsalmi Zn-Cu-Ag-Au VMS deposit in the Svecofennian domain of Finland has undergone various degrees of metamorphism and deformation, which have altered the composition and texture of the minerals, resulting in sulfide remobilization. However, studies on metamorphism and its influence on the ore mineral remobilization in the Pyhäsalmi region are lacking. Our study provides insights into the remobilization history of ore minerals during polyphase deformational and metamorphic events in the deposit halo region by integrating mineralogical, textural, mineral chemical, microtextural, and 3D micro-CT analyses. We propose that the Pyhäsalmi deposit has experienced two distinct ore mineral remobilization stages: (a) The first stage, associated with D_1-D_2 deformational phase, is dominated by solid-state (mechanical) remobilization processes demonstrated by cataclastic flow, foliated, elongated sulfide, which possibly occurred before the metamorphic peak denoted by staurolite + garnet + cordierite, and (b) The second stage, linked to D_4 deformational phase, is characterized by mixed-state remobilization processes evidenced by the spatial distribution of disseminated pyrrhotite around the grain boundaries of silicate porphyroblasts, attenuation of sulfides around the hinge zone of the crenulation cleavages and fracture filling sulfides, which possibly occurred during metamorphic peak conditions represented by sillimanite + garnet + cordierite + biotite. Published studies on ore remobilization often overlook the potential of linking ore minerals to metamorphic mineral assemblages through petrographic and microstructural observations. Our study addresses this gap by providing a framework to decode the ore mineral remobilization events in polyphase deformational and metamorphic environments using metamorphic mineral assemblages, garnet porphyroblasts, and microstructural analysis.

Keywords VMS deposit · Metamorphism · Garnet · Micro-CT · Remobilization · Svecofennia

Introduction

Volcanic massive sulfide (VMS) deposits are an important contributor to global base metals (Pb, Cu and Zn), precious metals (Ag and Au), and other metals (Cd, Se, Sn, Bi, Ge, Ga, and In; Franklin et al. 2005; Galley et al. 2007). These deposits are formed from the interaction of circulating hydrothermal fluids with wall rocks within extensional tectonic settings such as mid-ocean ridges, back-arc basins, and intra-oceanic arc rifts (Franklin 1993, 1996; Galley et al. 2007; Piercey 2010, 2011; Hannington et al. 2014). The majority of Precambrian VMS deposits often undergo varying degrees of metamorphism and deformation (Vokes 1969, 2000; McDonald 1970; Marshall and Gilligan 1987, 1993; Castroviejo et al. 2011; Cloutier et al. 2015; Duuring et al. 2016). Mosier et al. (2009) observed that out of 819 global VMS deposits, merely 3% are hosted in unmetamorphosed rocks. On the contrary, 62% are hosted in greenschist facies; 13% are hosted in contact metamorphism; 11% are hosted in amphibolite facies;

✉ Sk Rakibul Islam
rakibul.islam@utu.fi

[1] Department of Geography and Geology, University of Turku, Turku, Finland

[2] Geological Survey of Finland, Espoo, Finland

[3] Department of Physics and Astronomy, University of Turku, Turku, Finland

[4] Timalfi Partners Ay, Tampere, Finland

8.5% are hosted in sub-greenschist facies; 2% are hosted in blueschist or eclogite facies; 0.5% are hosted in granulite facies.

Metamorphism and deformation cause remobilization of sulfide deposits, which involves relocating and redeposition of ore constituents from the pre-existing deposits (Mookherjee 1976; Etheridge et al. 1984; Cox 1987; Knipe 1989; Rutter 1993; Marshall et al. 2000). The remobilization process can enhance metal tenor by coarsening the mineral grain size, which in turn improves the beneficiation potential (Marshall and Gilligan 1993). Moreover, intense remobilization may also result in the formation of new ore bodies (Gu and McClay 1992; Large 1992; Marshall et al. 2000). The remobilization process is generally achieved through solid-state, liquid-state, or mixed-state transfer processes (Etheridge et al. 1984; Cox 1987; Knipe 1989; Marshall et al. 2000). These processes change the brittle-ductile behavior of the ore minerals in metamorphic environments by various deformation mechanisms such as cataclastic flow, dislocation flow, diffusion mass transfer, solution transfer, grain-boundary sliding (Plimer 1984; Cox 1987; Marshall and Gilligan 1987, 1993; Barrie et al. 2007, 2009). This deformation often results in brecciated, elongated, folded, foliated and deformed minerals along with fracture-filling mineral assemblages (Vokes 1969, 2000; Plimer 1984; Cox 1987; Marshall and Gilligan 1987, 1993).

Thus, petrographical and mineralogical analyses of rock samples can yield critical constraints on remobilization mechanisms and can aid in defining the relative timing of these processes. Moreover, integrating petrography with 2D scanning electron microscopy (SEM) based mineral compositional analysis, complemented by 3D micro-CT imaging, provides a powerful tool to study elemental spatial distribution patterns. This coupled analytical approach can reveal microstructural controls on the formation and redistribution of sulfide minerals during deformation and metamorphic processes (Ketcham et al. 2005, 2010; Baker et al. 2012; Sayab et al. 2015, 2017; Corti et al. 2019). Micro-CT offers remarkable 3D visualization and analysis of metamorphic fabrics (i.e., foliation, lineation, and schistosity) and microstructures, providing insights into regional deformation (Denison et al. 1997; Ketcham and Carlson 2001; Ferré et al. 2014; Parsons et al. 2016). Garnet porphyroblasts predominantly display distinct inclusion patterns that preserve the rock's deformation history at the time of their growth (Bell and Johnson 1989; Johnson 1999; Timms 2003; Vernon 2018). Therefore, studying these porphyroblast microstructures, especially in 3D, can enable us to reconstruct the relative timing between mineral growth and deformation, providing insights into sulfide remobilization events.

The Vihanti-Pyhäsalmi region is a renowned host of Paleoproterozoic VMS deposits within the Fennoscandian Shield (Mäki 1986; Weihed et al. 2005; Laine et al. 2015; Fig. 1). The Pyhäsalmi Zn-Cu deposit is the largest VMS deposit in Finland with total extracted ore from the closed Pyhäsalmi mine exceeding 75.7 Mt, grading 1.9 wt.% Zn, 0.9 wt.% Cu, 0.4 g/t Au, and 14.1 g/t Ag (Imaña 2003; Mäki et al. 2015). The deposit extends vertically up to 1,420 m, hosted by altered rhyolitic and basaltic volcanic rocks (Fig. 2; Imaña 2003; Mäki and Puustjärvi 2003). The characteristic mineralization of this deposit is represented by a massive pyrite core surrounded by pyrite-chalcopyrite-calcite, which is capped by sphalerite-pyrite-barite-calcite (e.g., Imaña 2003). Pyrite is the most dominant sulfide of the whole ore body. The 1.93–1.91 Ga old Pyhäsalmi deposit and its host rock have experienced lower to upper amphibolite facies metamorphism and four phases of deformation (D_1-D_4), resulting in the remobilization of the primary Zn-Cu deposits (Vaasjoki and Sakko 1988; Korsman et al. 1997; Roberts et al. 2004; Laine et al. 2015; Mäki et al. 2015). The Pyhäsalmi deposit and its halo region have been extensively studied in regional geology and tectonic settings (Helovuori 1979; Roberts et al. 2004; Laitala 2015), in seismic reflection profiling (Heinonen et al. 2013), and in 3D subsurface modeling (Laine et al. 2015). While previous work by Laine et al. (2015) addresses constraints on remobilization of the primary ore, studies addressing metamorphism and its influences on sulfide remobilization history in the Pyhäsalmi halo region have not been carried out yet. Understanding the remobilization processes operating in this region can provide critical insights into mineral exploration. For deposits hosted in metamorphic rocks, detailed and systematic observations of ore mineral and host rock characteristics such as mineralogy, texture, and microstructure are an effective tool to unravel the relative timing between the ore mineral remobilization, halo region metamorphism, and deformation (Cartwright and Oliver 1998; Marshall et al. 2000; Zhong et al. 2015).

Firstly, we aim to decipher types of sulfide remobilization processes, distinguishing between solid-state, liquid-state, or mixed-state mechanisms. This is achieved by analyzing the microstructure and composition of pyrite, pyrrhotite, and occasional chalcopyrite and sphalerite from the alteration halo of the Pyhäsalmi VMS deposit. Secondly, we aim to determine the number of remobilization events, particularly whether multiple phases of remobilization occurred during the previously proposed regional polyphase deformational and metamorphic events in the studied area. This is accomplished by integrating the petrographic study of metamorphic mineral assemblages with microstructural analysis of sulfides and garnet porphyroblasts in 2D and 3D. Thirdly, we aim to deduce metamorphic conditions on the halo region based on mineral assemblages and texture. Lastly, we aim to correlate our microstructural study with the previously proposed regional deformational phases. The published ore remobilization studies often overlook the potential of linking ore minerals to metamorphic mineral assemblages using petrographic and microstructural observation to constrain the remobilization events and correlate it with the regional deformation and metamorphism. Our study addresses this oversight and provides a framework to decode the ore mineral remobilization events in polyphase deformational metamorphic environments.

Regional geology

Our study area, the Vihanti-Pyhäsalmi region is located between the Archean basement and the main phase of Paleoproterozoic Svecofennian crust in the Fennoscandian Shield (Fig. 1). The Vihanti-Pyhäsalmi region is proposed to have been formed by rifting of the Paleoproterozoic oceanic island arc (1.93–1.91 Ga; Mäki 1986; Gaál and Gorbatschev 1987; Ekdahl 1993; Lahtinen 1994; Kousa et al. 1994; Roberts et al. 2004; Laine et al. 2015). This region consists of variable supracrustal lithologies, mainly volcanic rocks, volcanic sedimentary rocks, and sediments, all of which are mainly metamorphosed from lower amphibolite facies to upper amphibolite facies conditions and locally

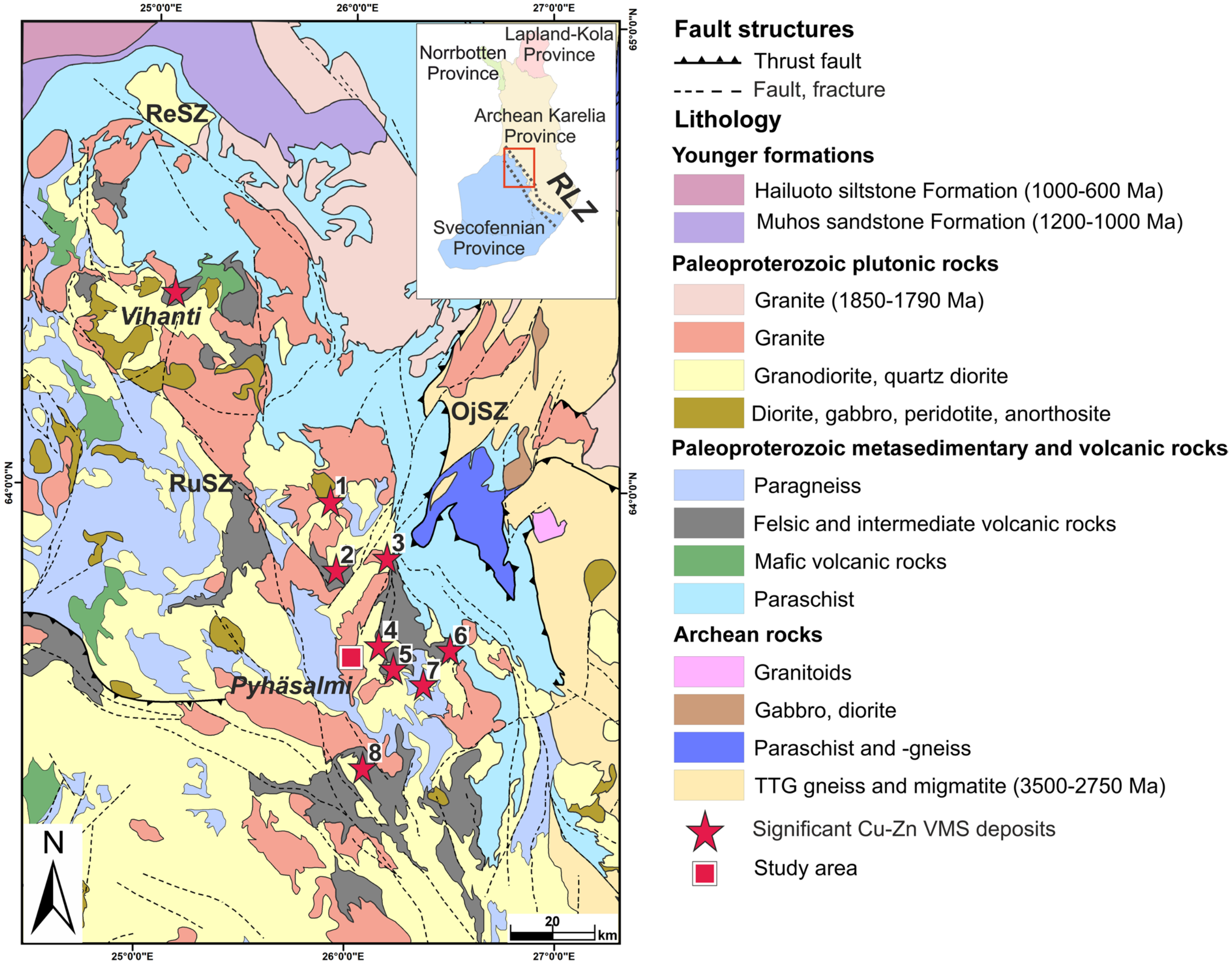

Fig. 1 Bedrock map of the Vihanti-Pyhäsalmi area around Raahe-Ladogga zone (RLZ). VMS mineralization sites of Vihanti and Pyhäsalmi region along with some important satellite deposits are marked with a *star* (based on Mäki et al. 2015). The base map is modified after Bedrock of Finland- DigiKP (Abbreviation: OjSZ = Oulujärvi shear zone, ReSZ = Revonneva shear zone, RuSZ = Ruhaperä shear zone, 1 = Vuohtojoki, 2 = Kaskela, 3 = Kokkopuro, 4 = Mullikkoräme, 5 = Konttikallio, 6 = Hallaperä, 7 = Kalliokylä, 8 = Kangasjärvi)

increasing to granulite facies conditions (Korsman et al. 1997). Moreover, the region hosts two large VMS deposits, namely Pyhäsalmi and Vihanti, along with several smaller massive sulfide deposits such as Mullikkoräme, Konttikallio, Kalliokylä, Kangasjärvi, Hallaperä, Vuohtojoki, Kaskela and Kokkopuro (Fig. 1; Laine et al. 2015). Some of these smaller deposits are satellite deposits that have been mined out, while others are considered uneconomic (Mäki et al. 2015). Based on variable volcanic environments, the older Svecofennian primitive island arc is divided into two economically important lithostratigraphical groups called Pyhäsalmi (1.93–1.92 Ga) and Vihanti (1.92 Ga) (Figs. 1 and 2a; Kousa et al. 1994, 2013). The lower Pyhäsalmi group represents bimodal-felsic metavolcanic sequences, whereas the upper Vihanti group is dominated by thick layers of intermediate and felsic metavolcanic rocks that were deposited during the continuous period of arc evolution. Regionally, these two stratigraphic units are separated by the NE-striking Oulujärvi shear zone (OjSZ) and two major southeast-northwest-striking faults i.e., the Revonneva (ReSZ) and Ruhaperä (RuSZ) shear zones (Fig. 1). The metavolcanic rocks of the Pyhäsalmi group are located in antiformal domes, whereas the overlying metavolcanic and metasedimentary rocks of the Vihanti group are found in a synformal basin (Fig. 2a). A subvolcanic tonalite intrusion in the antiformal structure of the Pyhäsalmi group is closely associated with the 1.93–1.91 Ga volcanic event (Fig. 2). Later, the volcanic sequences were intruded by the main phase of Svecofennian intrusive rocks during 1.89–1.87 Ga (Ekdahl 1993; Laine et al. 2015; Mäki et al. 2015; Fig. 2). The Pyhäsalmi VMS deposit is located in the upper part of the Pyhäsalmi group (Fig. 2a). Massive mafic meta-lavas that overlie the felsic metavolcanics form the uppermost part of the Pyhäsalmi group (Puustjärvi 1999; Roberts et al. 2004; Mäki et al. 2015). The inferred stratigraphy of the lowermost part of the group reveals the presence of

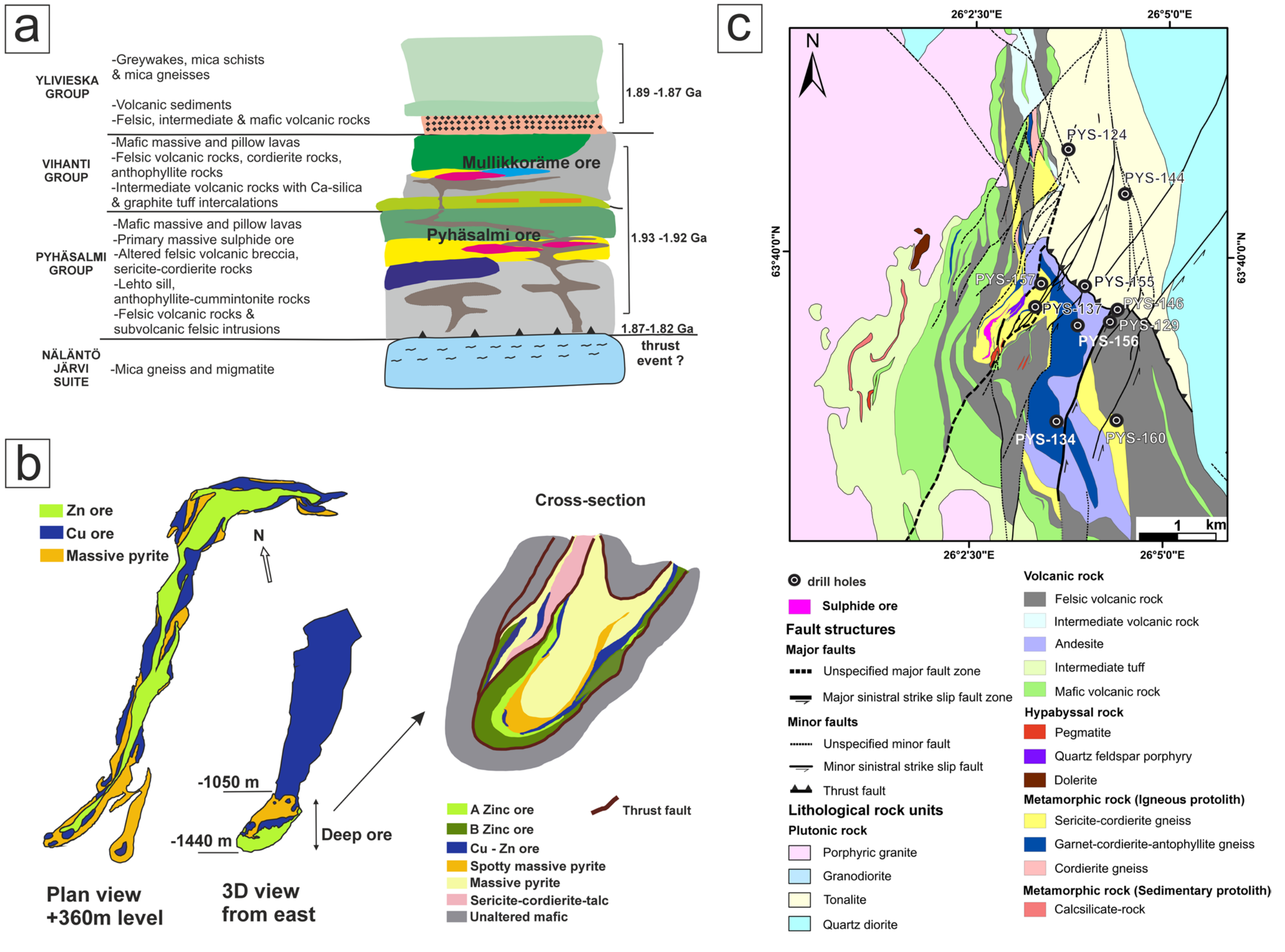

Fig. 2 Geology of the Pyhäsalmi VMS deposit. **a** Stratigraphy of the Pyhäsalmi area and stratigraphic position of the Pyhäsalmi ore body (modified after Mäki et al. 2015). **b** 3D, plan and cross-section view of the deep ore body mineral zonation (modified after Imaña 2003). **c** Bedrock location map of the studied samples around the Pyhäsalmi main sulfide ore deposit. The base map is modified after Bedrock of Finland-DigiKP

characteristically voluminous felsic metavolcanic rocks such as the pinkish grey Na-rich quartz-plagioclase-porphyritic rhyolitic rocks (Kousa et al. 2013). This unit is overlain by a highly altered and metamorphosed voluminous felsic pyroclastic unit with brecciated rocks. This pyroclastic unit is metamorphosed into cordierite-sericite schist and hosts the Pyhäsalmi deposit (Fig. 2a). The Pyhäsalmi ore deposit is subdivided into two parts, separated by a shear zone characterized by talc-sericite alteration: the steeply dipping, elongated, conical shape upper ore body and the sub-rounded bulbous deep ore body (Imaña et al. 2003, Fig. 2b). The upper body is 150–650 m wide, 10–60 m thick, and extends from the surface to about 1100 m depth. This part of the ore body consists of sub-vertical intercalations of Zn- and Cu-bearing pyritic ore (Fig. 2b). However, the upper ore body lacks mineral zonation due to deformation and post-VMS tectonic stacking of the original massive sulfide body (Helovuori 1979; Meriläinen 1985; Mäki et al. 2015). The deep ore body is 300–400 m wide, 200–300 m thick and located at depths between 1000 and 1400 m, exhibiting typical VMS mineral zonation (Imaña 2003; Mäki et al. 2015; Fig. 2b). This zonation (Fig. 2b) includes (1) a barren massive pyrite core characterized by 0.2–2.0 cm pyrite porphyroblast and 90–95% sulfides, (2) spotty massive pyrite with intergranular chalcopyrite enveloping the barren massive core shows colloform banding, replacement textures and 70–85% sulfides, (3) Cu-rich pyrite zone with recrystallized sphalerite in the middle and the external part of the deep ore exhibiting cataclastic fracturing, breccias, chalcopyrite disease and 90% sulfides, (4) A Zinc zone surrounding the spotty pyrite represented by banded, brecciated, disseminated pyrite, sphalerite and magnetite with 40–60% sulfide content, and (5) B Zinc zone at the periphery of the ore showing rounded, sheared mylonitic pyrite porphyroclasts in sphalerite, barite, quartz matrix and $>60\%$ sulfides content (Imaña 2003; Laitala 2016). Pyrrhotite mostly occurs in areas of pegmatite contact and ductile shear zone (Fig. 2c). The alteration zone surrounding the upper ore body is tectonically controlled but pervasive and widespread for about 4 km in the north–south direction and to a depth beyond 1 km (Meriläinen 1985; Imaña 2003). The alterations are represented by mineral assemblages of quartz-cordierite-biotite-muscovite-barite (Fig. 2c) related to strong alkali depletion and enrichment in Fe, K, Mg, Si, and Ba, whereas the deep ore body is surrounded by weakly altered volcanic sequences represented by tectonically banded felsic and mafic schist (Imaña et al. 2003). However, remobilization of Au and As surrounding the deep ore body is common due to the intrusion of several unaltered mafic dikes (Mäki et al. 2015).

Structural evolution of the Vihanti-Pyhäsalmi region

The pre-compressional stage in the Vihanti-Pyhäsalmi region is defined by the deposition of epicontinental sediments and the formation of primary massive sulfide ore along the present-day western margins of Archean basement rocks, occurring before 1.91 Ga (Fig. 1). The proposed structural evolution of the Vihanti-Pyhäsalmi region by Laine et al. (2015) is attributed to two compressional stages separated by intermittent extensional phases. The initial compressional stage consists of three distinct deformational phases (D_1–D_3), while the second compressional stage is marked by a single deformational phase (D_4).

The initial compressional stage (D_1-D_3) was initiated by thrusting the earlier flat-lying epicontinental sedimentary strata towards the Archean basement in the northeast at approximately 1.91 Ga. This resulted in the formation of parautochthonous-autochthonous nappes on the Archean basement as well as the early thickening and remobilization of the VMS ore. During the D_1-D_2 phase, the older Svecofennian volcanic arc probably collided with the Archean basement and the earlier nappes are causing a NW–SE-striking major thrust fault zone between the Svecofennian and Archean units (Huhtala 1979; Korsman et al. 1988; Laine et al. 2015). This major thrust zone is known as the Raahe-Ladoga zone, which has reactivated several times after subsequent orogenic movements with current surface exposure revealing mainly dextral movements (Roberts et al. 2003). The movement and deformation of the D_1-D_2 phase caused continual high-strain deformation, resulting in folding of contrasting competency material along the shear zone. Further, presence of the massive sulfide body at Pyhäsalmi stratigraphy might have acted as a strain concentrator, possibly producing a higher amplitude fold. The continuous deformation of this higher amplitude structure resulted in stretching and shearing of the ore body and the subsequent formation of localized sheath folds of the massive sulfide ore body (Laine et al. 2015; Mäki et al. 2015). This sheath fold caused the deep ore body to be tectonically displaced onto less altered mafic volcanic rocks of hanging wall. Later folding and tilting resulted in the whole massive sulfide ore body being enclosed within unaltered rocks (Fig. 2). During D_1-D_2 phase, contemporaneous volcanic activity (1.89–1.85 Ga) along the RLZ, intruded into the older island arc, resulted in high temperature-low pressure metamorphism with peak conditions at 600 °C/4–5 kbar estimated by Korja et al. (1994) (Fig. 2). The later D_3 phase at 1.85 Ga caused continuous SW-NE compression, which led to tectonic thickening and refolding of the earlier phase's flat-lying structures into an upright position along the RLZ, as well as recrystallization of sulfide ore as proposed by Laine et al. (2015). The end of the D_3 phase is denoted by the development of a large-scale vertical shear zone along the edge of the Archean basement. Finally, the intermittent extensional phases (1.85–1.82 Ga) emplaced large volumes of orthopyroxene-bearing granites into the folded strata and uplifted the granulite facies metamorphic rocks of the older Svecofennian island arc along the earlier shear zone in the Svecofennian domain (Figs. 1, 2; Korsman 1984; Hölttä 1988). After cessation of extensional phases, the second compressional stage (D_4, between 1.82 and 1.79 Ga) shifted the earlier SW-NE compression direction to N-S, which caused the refolding of the earlier D_3 folds into a new set of large-scale SW-NE-striking D_4 folds and the formation of a basin-dome interference structure in the Vihanti-Pyhäsalmi region. This N-S directional shift resulted in overall dextral movement of the RLZ shear zone (Kärki et al. 1993). Moreover, the prominent structure of D_4 stage is the formation of the crustal scale, sinistral, SW-NE-striking Oulujärvi Shear Zone (OjSZ; Fig. 1). The Vihanti-Pyhäsalmi region experienced intense shearing caused by horsetail system of the OjSZ shear zone, which led to the final remobilization of the Pyhäsalmi massive sulfide ore. According to Laine et al. (2015), the ore body has undergone two-stage remobilization, i.e., the initial remobilization during the D_1-D_2 phase (1.91 Ga) and the second during the D_4 phase (1.82–1.79 Ga). During the D_4 phase, the activation of earlier shear zones along the Archean craton resulted in intrusions of late-stage granites proximal to the major shear zones, as well as intrusions of pegmatite granite at the eastern side of the Pyhäsalmi ore deposit (Fig. 2). These pegmatite granite plutons along the active fault zone led to metasomatic alteration, consequently forming skarns. Moreover, the active fault zones provided conduits for hydrothermal fluids, which facilitated remobilization of the Au and galena close to the ore deposit during the D_4 phase (Figs. 1, 2a; Mustonen 1998; Mäki et al. 2015).

Methods

Petrographic study

A lithological study of the drill cores was conducted at the Pyhäsalmi mine drill core facility from eleven drill cores (Fig. 2c). A description of the samples is presented in Electronic supplementary material 1. To investigate halo region sulfide remobilization in tectono-metamorphic environments, the drill core samples were selected from within the Pyhäsalmi deposit alteration halo, proximal to faults. The selected drill cores are within 3 km from the ore body (Fig. 2c). The petrographic analyses were performed on 93 polished thin sections made from the drill cores for identifying the ore and metamorphic mineral assemblages, as well as their texture under the polarized and reflected light microscope. The studied thin sections were prepared at the Geological Survey of Finland, Kuopio and the University of Turku.

SEM analysis and imaging

Elemental analysis using scanning electron microscopy (SEM) was conducted on nine polished thin sections, five of which were from drill core samples previously analyzed by micro-CT imaging (Electronic supplementary material 1). The thin sections were sputter-coated with carbon to ensure electrical conductivity (Q150 V ES +, Quorum Technologies, United Kingdom). Backscatter electron (BSE) imaging and energy-dispersive X-ray spectroscopy (EDS) elemental mapping were performed using an Apreo S field-emission SEM (Thermo Scientific, The Netherlands), equipped with an UltimMax 100 EDS silicon drift detector (Oxford Instruments, United Kingdom) at the Department of Physics and Astronomy, University of Turku. Data analysis was carried out using AZtec v6.1 software (Oxford Instruments). Images and elemental data were acquired at an accelerating voltage of 20 kV. Large-area BSE and EDS maps were generated by automated stitching of higher-magnification micrographs. Additionally, EDS spectra for specific points of interest were collected separately to analyze compositional variations in sulfides. For the point analysis, the electron beam current was set to provide approximately 100 kcps output count rate at a dead time of 20–25%, collecting 1.5 million counts per spectrum. Spectral artefacts and overlaps were resolved utilizing software built-in pulse pile-up correction along with filtered least squares fitting for background removal and peak deconvolution, whereas estimation of the relative composition is done by XPP-φ(ρz) matrix correction in the AZtec software.

Micro-CT

3D fabric analysis from seven drill core samples was performed using X-ray microcomputed tomography (micro-CT), a modern-day nondestructive technology. The computed microtomography instrument used in this study is a GE phoenix v|tome|x s at the Geological Survey of Finland, Espoo. The samples were imaged for a full 360° rotation with a varying number of steps. At each step, the detector waited for a single exposure time and then took an average of three exposures. No ring artefact reduction was used for any of the samples. The imaging parameters for different samples are presented in Electronic supplementary material 2. The tomographic slices were reconstructed by GE phoenix datos|× 2 reconstruction with variable isotropic voxel sizes for different samples (Electronic supplementary material 2). 3D image analysis (i.e., 3D visualization, rendering, volume segmentation, phase segmentation, fabric orientation and distribution) was done by Thermo Scientific PerGeos 2020.2 software. Contrasting gray scale values and texture in the 3D images enabled us to segment and separate the minerals of interest. Mineral phases (i.e., garnet, inclusion within garnet, matrices, sulfide) were separated using the marked-based watershed segmentation recipe. The porphyroblast of garnet, cordierite, quartz, anthophyllite and sulfide were identified. Furthermore, thin sections were made from the drill cores to confirm the mineralogy using a petrographic microscope. In addition to the volume of sulfide in garnet, the volume fractions of garnet and sulfide in the sample were also computed. The size distribution of garnets and sulfides was measured by fitting an ellipse with mutually perpendicular long (X), intermediate (Y) and short (Z) axes using the label analysis tool. Moreover, the spatial distribution of garnet and sulfide was visualized in different slices of rendered 3D images as well as documented in animated videos.

Results

Petrographic results

The studied samples comprise supracrustal rocks that represent highly altered and metamorphosed felsic and mafic volcanic rocks with aluminum silicate-rich altered turbidite interlayers, often containing visible porphyroblasts and ore minerals. The hydrothermal alteration is dominantly represented by chlorite, biotite and sericite alteration of biotite, cordierite, plagioclase, alkali feldspar, occasionally anthophyllite and hornblende (Fig. 3). Porphyroblasts of inclusion-rich garnets (up to 1.5 cm in diameter) and cordierites (up to 1.3 cm in diameter) are common and generally embedded between schistose mica-rich layers often implying metasedimentary interlayers (Fig. 4). Anhedral to subhedral cordierites are frequently pinitized (Fig. 4e). Ore minerals, i.e., pyrite, pyrrhotite, chalcopyrite, magnetite, ilmenite, and occasionally sphalerite occur as the major minerals of the halo region. The distinct metamorphic mineral assemblages of this region are characterized by (a) cordierite-quartz-biotite-chlorite; ((b) garnet-cordierite-biotite-sillimanite (fibrolite); (c) cordierite-anthophyllite-biotite-muscovite-chlorite; (d) cordierite-plagioclase-quartz-sillimanite and occasionally (a) hornblende-biotite-cordierite; (b) garnet-staurolite-cordierite. (Fig. 4). The cordierite-quartz-muscovite-biotite mineral assemblages are also common in the massive ore body alongside the chlorite-sericite alteration of plagioclase (Imaña 2003; Miettinen 2011). The main part of the altered rocks is dominantly muscovite-quartz and muscovite-quartz-cordierite (altered felsic volcanic rocks) occurred from the surface to a depth of about 300 m in the studied halo region of the Pyhäsalmi deposit. Moreover, zircon, titanite (± rutile), apatite, allanite and monazite are present only as accessory minerals. The anhedral to subhedral quartz grains show undulating extinction. The presence of stretched and elongated quartz grains in schistose samples is typical (Fig. 4c, f). The boundaries of subhedral to euhedral quartz and biotite grains intersect at an approximate angle of 120° exhibiting granoblastic texture (Fig. 3a). Prismatic anthophyllite (3–7 mm in diameter) and fibrolite sillimanite (0.1–1 mm in diameter) exhibit oriented linear fabric occasionally representing nematoblastic texture (Fig. 3b). The parallel alignment of the platy and elongated mica grains exhibits foliation imparting schistosity (Fig. 4c, d). Alternate layers of biotite, chlorite and anthophyllite with quartz, plagioclase and cordierite produce foliations forming gneissose structure.

Garnet types

Garnet porphyroblasts of 3–7 mm diameter are abundant from the halo region, predominantly occurring in Al-rich schistose mica layer. Most of the studied garnets are inclusion-rich and have experienced plastic deformation and later brittle fractures (Fig. 4). We have defined six distinct types of garnet based on their morphology and distribution pattern of the inclusion trails, i.e., from rim to core and internal–external foliation (S_i-S_e) relationship (Fig. 4; Table 1). Among these garnet types, Type-1 (cataclastic), Type-3 (rotated pre-kinematic) and Type-4 (syn-kinematic stretched), generally associated with schistose sheared mica-rich samples, are common. However, Type-2 (corona), Type-5 (cluster) and Type-6 (rounded overgrowth) are common in quartzo-feldspathic rich gneissic and schistose samples which are relatively less sheared.

Type-1 garnets are characterized by euhedral to subhedral, σ-type fragmented, angular grains with pressure shadow zones of quartz (1–3 mm in diameter) and cordierite (less than 2 mm in diameter) (Fig. 4a; Table 1). Occasionally, fragments of this garnet type are surrounded by rims of cordierite and mica grains. These garnet porphyroblasts (3–9 mm in diameter) contain inclusion trails of quartz, biotite, ilmenite needles (rutile), monazite and sulfides (i.e., pyrite, pyrrhotite and chalcopyrite). The garnet fragments are rotated, with inclusion trails displaying variable alignment relative to the external foliation (Fig. 4a; Table 1). *Type-2 garnets* are euhedral and vary from rounded to elliptical in shape. A notable feature of these garnet porphyroblasts (up to 1 mm in diameter) is the presence of prominent corona rims. These rims typically consist of quartz around garnet,

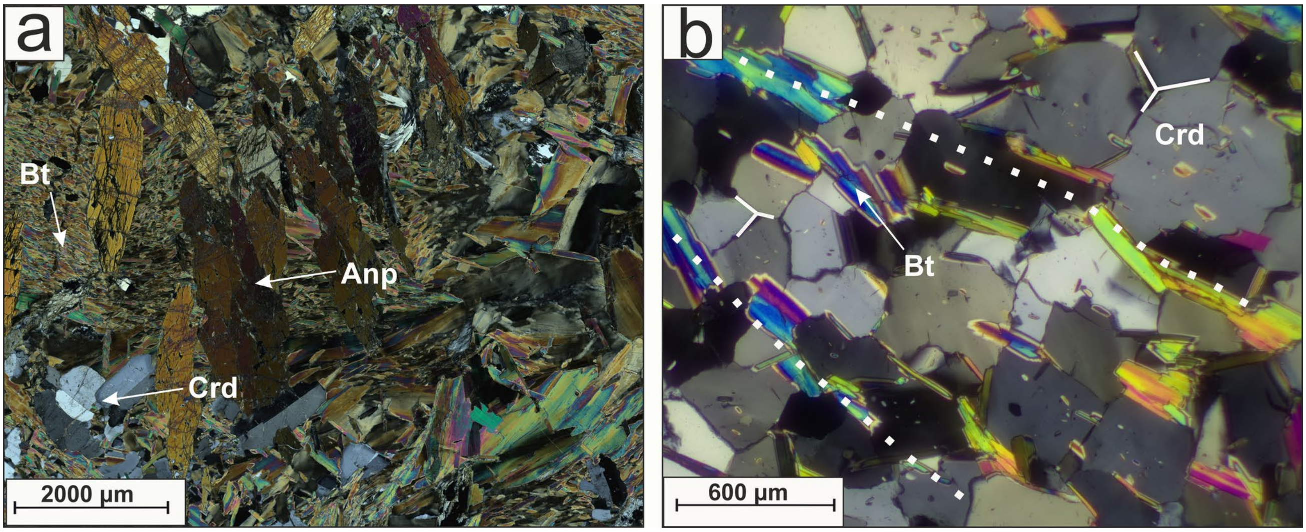

Fig. 3 Photomicrographs of metamorphic textures in Pyhäsalmi region. **a** Prismatic anthophyllites exhibiting nematoblastic texture under crossed polarizer. **b** Cordierite grains showing granoblastic texture; straight grain boundary of cordierite often is in 120° angular position with biotite and cordierite grains (Abbreviations: Bt – Biotite, Crd –Cordierite, Anp – Anthophyllite)

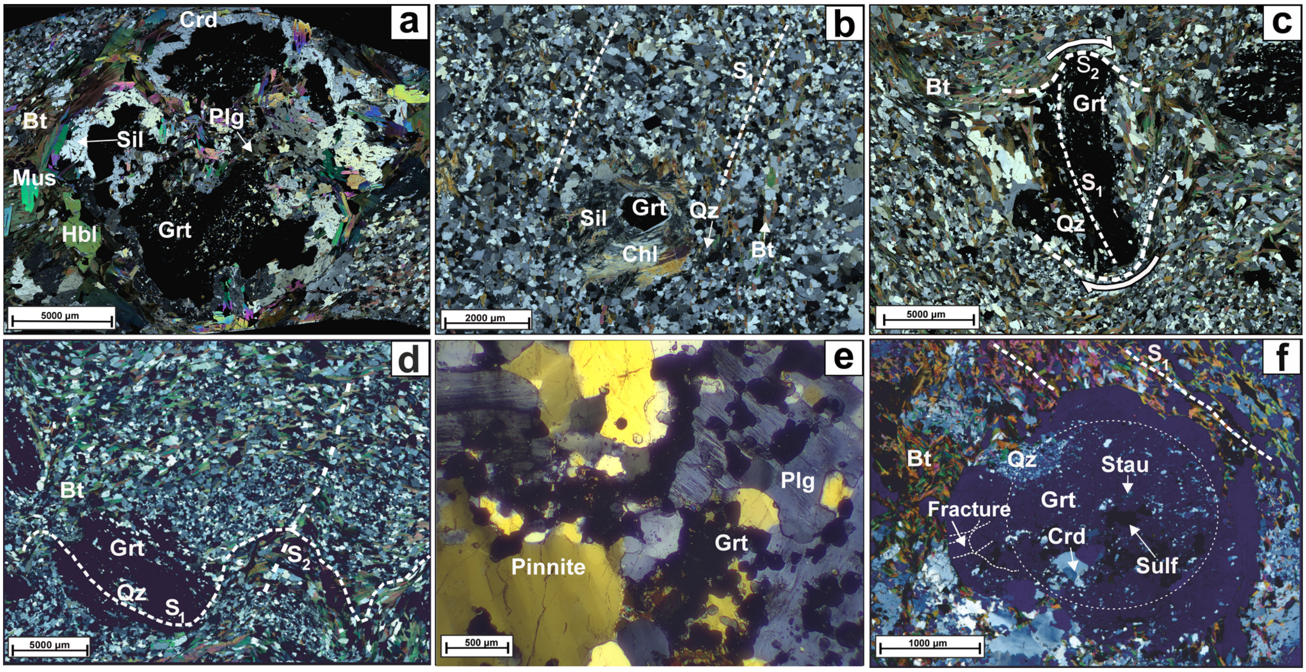

Fig. 4 Photomicrographs of distinct garnet porphyroblasts under cross-polarized light. **a** Type-1 cataclastic garnet from sample PYS-144(A); amphibolite facies fractured garnet porphyroblast, showing cataclastic deformation. **b** Type-2 corona garnet from PYS-124(A); euhedral shape garnet showing conspicuous rim of quartz, sillimanite and chlorite represents multiple metamorphic events i.e. prograde metamorphism followed by later retrograde alteration by presence of chloritization of sillimanite rim; **c** Type-3 rotated and deformed garnet from sample PYS-155(B); elongated deformed garnet rotated around mica (biotite) foliation forming pressure shadow zone. **d** Type- 4 syn-kinematic garnet from sample PYS-157(A), inclusion pattern within the garnet following continuity of external S_1 foliation which reveals syn-kinematic growth of the garnet, the garnet grows along the limbs of the crenulation cleavage; **e** Type-5 garnet clusters from sample PYS-155(E); clusters of less than millimeter sized garnets inclusion within plagioclase and cordierite. **f** Type-6 rounded garnet characterized by staurolite inclusion from sample PYS-157(B). This type of garnet has an inclusion-rich core represented by a white circle in the figure (Abbreviations: Grt – Garnet, Hbl – Hornblende, Plg – Plagioclase, Bt – Biotite, Qz – Quartz, Crd – Cordierite, Chl – Chlorite, Sil – Sillimanite, Mus – Muscovite, Sulf – Sulfide, Stau – Staurolite)

followed by sillimanite or a rim of quartz, followed by chlorite and sillimanite (Fig. 4b; Table 1). Although this garnet type is inclusion-free, inclusions of pyrite (less than 1 mm in diameter) and quartz can occasionally be observed around the rim of the garnet. These garnet porphyroblasts are mostly embedded in quartz-feldspar-rich matrix. *Type-3 garnets* appear as subhedral to euhedral grains that are bent, elongated, sheared and rotated. These porphyroblasts typically range from 2 to 6 mm in diameter and display subvertical inclusion trails of elongated quartz, biotite, ilmenite needles and sulfides (mainly pyrite and pyrrhotite) aligned with the external S_2 foliation of mica grains (Fig. 4c; Table 1). The internal S_1 foliations with inclusion trails are truncated by the S_2 external foliations. These garnets are mostly embedded in folded and sheared mica-rich layers which facilitate the rotation of the garnets. *Type-4 garnets* are subhedral to euhedral, elongated, and stretched, ranging from 3 to 6 mm in diameter. These garnets are typically found along the limbs of the crenulation cleavages (Fig. 4d; Table 1). They contain parallelly aligned inclusion trails (i.e., S_1 foliations) of quartz, cordierite, biotite, monazite, ilmenite needles, and sulfides (including pyrite, pyrrhotite, and chalcopyrite), all less than 1 mm in size. The parallel inclusion trails exhibit the continuity pattern of the external S_1 foliations which implies syn-kinematic growth history of this garnet type (Fig. 4d; Table 1). *Type-5 garnets* appear as clusters of rounded, euhedral grains and are relatively smaller in size compared to other types, less than 1 mm in diameter. This type of garnet is often found as inclusions within cordierite, plagioclase, and quartz (1–5 mm in diameter; Fig. 4e; Table 1). The characteristic feature of this cluster-type garnet is attributed to the absence of surrounding mica-rich layer, contrasting with other types of garnet that typically occur in such layers. Additionally, this garnet type is devoid of inclusion. *Type-6 garnets* are subhedral to euhedral, fractured, rounded grains, ranging from 2 to 7 mm in diameter. This garnet type has the presence of staurolite inclusions (less than 1 mm in diameter) and an inclusion-free rim (Fig. 4f; Table 1). The core of these garnet porphyroblasts is densely packed with inclusions of staurolite, quartz, polycrystalline quartz, cordierite, biotite, ilmenite needles, and elongated sulfides (including pyrite, pyrrhotite, and chalcopyrite). Inclusion trails of elongated sulfides are often aligned sub-vertically relative to external foliation (Fig. 4f; Table 1).

Sulfides and oxides

The studied samples from the halo region are characterized by the occurrence of ore minerals, including sulfide and iron-oxide minerals, which primarily appear as disseminated and often brecciated textures (Fig. 5a, d). The disseminated sulfides commonly occur along the grain boundaries of silicate porphyroblasts (e.g., garnet, cordierite). In contrast, sulfides such as pyrrhotite and chalcopyrite are frequently observed filling fractures and cracks, particularly in schistose samples. Additionally, folded sulfide banding is occasionally noted in these samples. The ore minerals typically consist of pyrite and pyrrhotite as major phases, with occasional magnetite, whereas chalcopyrite, sphalerite, and ilmenite occur as minor phases. Based on morphology, texture, and microstructure under reflected light, three types of pyrite and three types of pyrrhotite are identified. *Pyrite 1* occurs as *rounded and lath-shaped*, characterized by subhedral to anhedral inclusions (0.1–0.5 mm in diameter) within silicates (Fig. 5a). *Pyrite 2* includes euhedral to subhedral cubic crystals (0.3–2 mm in diameter) that are typically inclusion-poor and often with rounded or broken corners. These grains are typically found in contact with or as inclusions within silicate minerals, pyrrhotite, and sphalerite (Fig. 5h). This type occasionally displays a *durchbewegung* texture where pyrite crystals are present in a pyrrhotite matrix (Fig. 5b). *Pyrite 3* can be found as folded and fracture fillings crystals, characterized by deformed folded subhedral to anhedral grains (≤ 0.1 mm in diameter; Fig. 5c). *Pyrrhotite 1* is sub-rounded and elongated, anhedral to subhedral disseminated grains (0.3–0.4 mm in diameter) that are typically in contact with silicate minerals such as cordierite, quartz, biotite, garnet (Fig. 5d, e). *Pyrrhotite 2* forms subhedral to anhedral cubic grains 0.3–1.0 mm in diameter with rounded corners and are rich in inclusions such as pyrite, chalcopyrite, biotite, quartz, unidentified and unreflected mineral grains (Fig. 5e). *Pyrrhotite 3* is represented by subhedral to anhedral, elongated, folded grains that are foliated and inclusion-rich (i.e., pyrite, chalcopyrite, biotite, and unidentified minerals; Fig. 5f). Chalcopyrite appears predominantly as inclusions within pyrrhotite and pyrite especially in pyrite 3, pyrrhotite 2 and pyrrhotite 3 (Fig. 5g). Cubic euhedral crystals of magnetite (0.3–3.0 mm in diameter) are also present (Fig. 5i) in some of the interlayers, occasionally with elongated, needle-like ilmenite that often shows intergrowth with magnetite.

SEM–EDS results

SEM–EDS elemental maps of all garnets show homogenous elemental distribution and lack of elemental zoning (Table 1 in Electronic supplementary material 3). In the garnet compositional ternary diagrams (modified after Coleman et al. 1965), the studied garnet types are visualized (Fig. 6a). All six types plot to the Fe–Mn rich corner, indicating dominantly almandine-spessartine (Fe + Mn) type that is typical for amphibolite facies conditions (Dempster et al. 2017). However, Type-5 relatively inclusion-poor garnets that are enclosed within cordierite and plagioclase are compositionally Mg-poor and Ca-rich (Fig. 6a). This depletion of Mg is probably due to the formation of the cordierite that encloses the garnet porphyroblasts.

The Pyhäsalmi area sulfide minerals from the studied thin sections show homogenous composition without zoning in SEM–EDS spectral analysis (Fig. 6b; Table 2 in Electronic supplementary material 3). The composition of sulfide minerals does not vary between different lithologies or different morphic types (Tables 2, 3 in Electronic supplementary material 3). We analyzed sulfide inclusions in garnet porphyroblasts and within the matrix. The inclusions are represented by pyrite (1 and 2), pyrrhotite 2, and chalcopyrite. The iron and sulfur contents of pyrite are homogeneous both in inclusions (Fe: 44.52–47.41 wt%; S: 52.59–55.48 wt%) and within matrix (Fe: 46.21–48.54 wt%; S: 51.46–53.79 wt%; Fig. 7a). Despite overlapping, the iron content of pyrite is marginally higher in inclusions (inclusion: 46.21–48.54 wt%; matrix: 44.52–47.41 wt%), whereas sulfur exhibits a reverse distribution pattern (inclusion: 52.59–55.48 wt%; matrix: 51.46–53.79 wt%). SEM–EDS analysis of pyrrhotite from the metamorphosed altered volcanic rocks of Pyhäsalmi shows a mostly homogeneous distribution of iron and sulfur both for inclusion (Fe: 59.0–63.09 wt%; S: 36.91–41.0 wt%) and within matrix (Fe: 60.2–61.91 wt%, S: 38.09–39.8 wt%) (Fig. 7b). Additionally, chalcopyrite shows marginally higher Cu content for inclusion compared to within matrix (inclusion: 32.77–35.77 wt%; matrix: 33.60–34.20 wt%; Fig. 7c). Cubic euhedral magnetites are often vanadiferous (0.33–0.57 wt%) and occur as disseminated grains in some of the quartz-cordierite-biotite-chlorite-rich

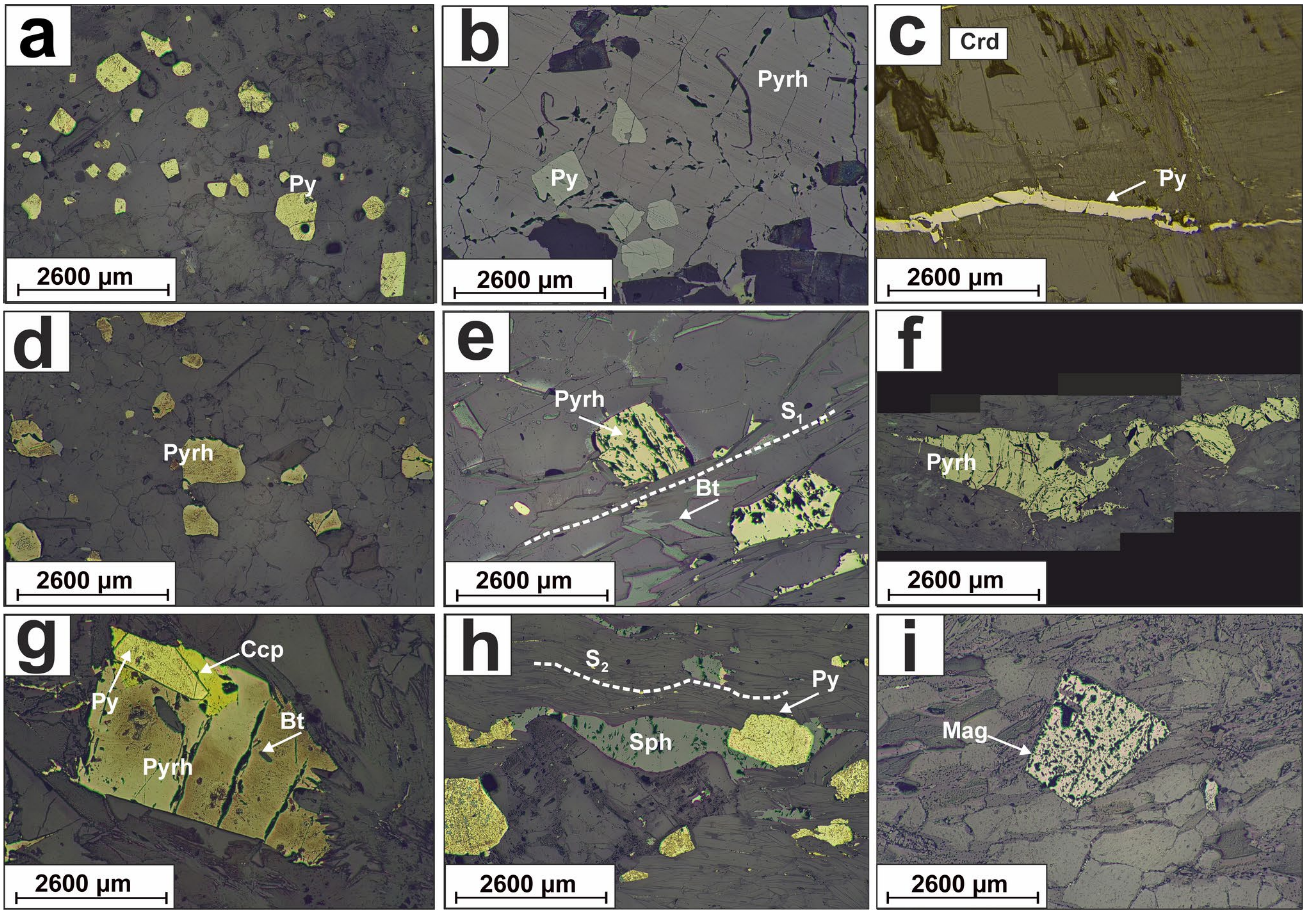

Fig. 5 Photomicrographs of sulfide distinct morphic types under reflected light. **a** Pyrite 1: subrounded, cubic, lath-shaped disseminated pyrite grains from sample PYS-157(D). **b** Pyrite 2: cubic crystals of pyrite grains in pyrrhotite matrix reflect durchbewegung texture from sample PYS-155(D). **c** Pyrite 3: folded crack and fracture filling pyrite during low temperature prevailing condition indicates retrograde metamorphic environment PYS-157(C). **d** Pyrrhotite 1: sub-rounded disseminated pyrrhotite grains from sample PYS-155(C). e) Pyrrhotite 2: inclusions rich cubic pyrrhotite grain from PYS-155(C). **f** Pyrrhotite 3: deformed, folded, elongated inclusion-rich pyrrhotite from PYS-144(B). **g** Lath-shaped pyrite and chalcopyrite inclusions in cubic pyrrhotite from sample PYS-155(B); pyrrhotite also has inclusions of elongated biotite. **h** Fragmented cubic pyrite inclusion in deformed folded sphalerite from sample PYS-155(A). **i** Inclusion-rich cubic magnetite crystals from sample PYS-134(A) (Abbreviations: Py – Pyrite, Crd – Cordierite, Pyrh – Pyrrhotite, Ccp – Chalcopyrite, Sph – Sphalerite, Mag – Magnetite, Bt – Biotite)

layers (Table 2 in Electronic supplementary material 3). These magnetite crystals have occasionally intergrown with elongated, needle-like ilmenite which has a high Ti content (up to 30.68 wt%) (Fig. 5i; Table 2 in Electronic supplementary material 3). Moreover, disseminated sphalerite grains are occasionally embedded in cordierite-garnet-biotite-rich layers. Sphalerite inclusions inside garnets have a higher zinc content than in the matrix (inclusion: 58.52 wt%; matrix: 55.43–56.78 wt%). Additionally, the SEM–EDS analysis of pyrite-sphalerite inclusions inside the garnet exhibits cadmium enrichment in sphalerite (9.13 wt%; Table 2 in Electronic supplementary material 3).

Micro-CT results 3D visualization, segmentation, and quantitative analysis

The selected seven drill core samples for the micro-CT represent texturally and lithologically variable supracrustal rocks. Samples from PYS-129 show anthophyllite, magnetite-rich supracrustal rocks along with banded pyrite intercalation with quartz at a depth of over 1000 m, whereas samples from PYS-144 exhibit folded and deformed biotite and sulfides with chlorite alteration (Electronic supplementary material 1). On the other hand, samples from PYS-155 consist of biotite-garnet-rich supracrustal rocks with disseminated sulfides, occasionally containing pyrite within massive pyrrhotite reflecting durchbewegung texture (Electronic supplementary material 1).

The different mineral assemblages (i.e., sulfides, oxides, garnets and silicate matrices) are visualized based on variable morphologies, textures in 3D images after reconstructing the micro-CT data from the selected drill core samples of the halo region (Fig. 8a, b). Additionally, the contrasting gray scale values in the 3D images enable us to separate dense mineral assemblages (i.e., the bright regions) from relatively less dense mineral assemblages (i.e., the dark regions) (Fig. 8a, c; Table 6 in Electronic supplementary material 3). The brightest regions are dominantly attributed to the sulfide and oxide minerals from the studied samples, followed by silicate porphyroblasts (i.e., garnets) (Fig. 8a, c; Table 6 in Electronic supplementary material 3). However, the distinction between various denser minerals (i.e., sulfides and oxides) was not successful using solely gray scale contrast values. The darker regions in the reconstructed gray scale images refer to the silicate matrices (i.e., mica and anthophyllite aggregates) (Fig. 8a, c; Tables 4–8 in Electronic supplementary material 3). However, only shape-based analysis was occasionally successful in differentiating distinct silicate matrices such as columnar-diamond shape of anthophyllite and platy elongated micas. These mineral identifications were confirmed through thin section petrographic study. On the other hand, the darkest regions are assigned to quartz-cordierite-feldspar (Fig. 8a, c; Tables 4–8 in Electronic

Table 1 Garnet type based on its morphology, inclusion types and inclusion patterns (Fig. 4)

Garnet type	Morphology	Texture	Inclusions	Inclusions pattern relative to external foliation
Type 1	Cataclastic σ	Euhedral to subhedral, 3–9 mm in diameter, rotated and fragmented, pressure shadow zones of quartz and cordierite	Quartz, biotite, ilmenite, monazite, sulfides	Variable alignments in rotated, fragmented grains
Type 2	Corona	Euhedral, up to 1 mm in diameter, rounded to elliptical in shape, presence of reaction rims of quartz, sillimanite, chlorite	Inclusion-free; occasionally pyrite and quartz	Around rim of the garnet
Type 3	Rotated pre-kinematic	Subhedral to euhedral, 2–6 mm in diameter, elongated, rotated, stretched	Quartz, biotite, ilmenite, pyrite and pyrrhotite	Subvertical internal S_1 foliation, truncated by S_2 external foliation (mica)
Type 4	Syn-kinematic stretched	Subhedral to Euhedral, 3–6 mm in diameter, elongated, stretched, occur along the limbs of the crenulation	Quartz, cordierite, biotite, monazite, ilmenite, Pyrite, pyrrhotite, chalcopyrite, all less than 1 mm in size	Parallel alignment and continuity of external foliation
Type 5	Clusters	Euhedral, less than 1 mm in diameter, rounded, occur as inclusions in cordierite, plagioclase, quartz	Devoid of inclusion	—
Type 6	Rounded overgrowth	Subhedral to euhedral, 2–7 mm in diameter, rounded, overgrowth; inclusions free rim	Characteristics staurolite and calcite inclusions; additionally, polycrystalline quartz, cordierite, biotite, ilmenite, pyrite, pyrrhotite, chalcopyrite	Subvertical alignment of especially elongated sulfides

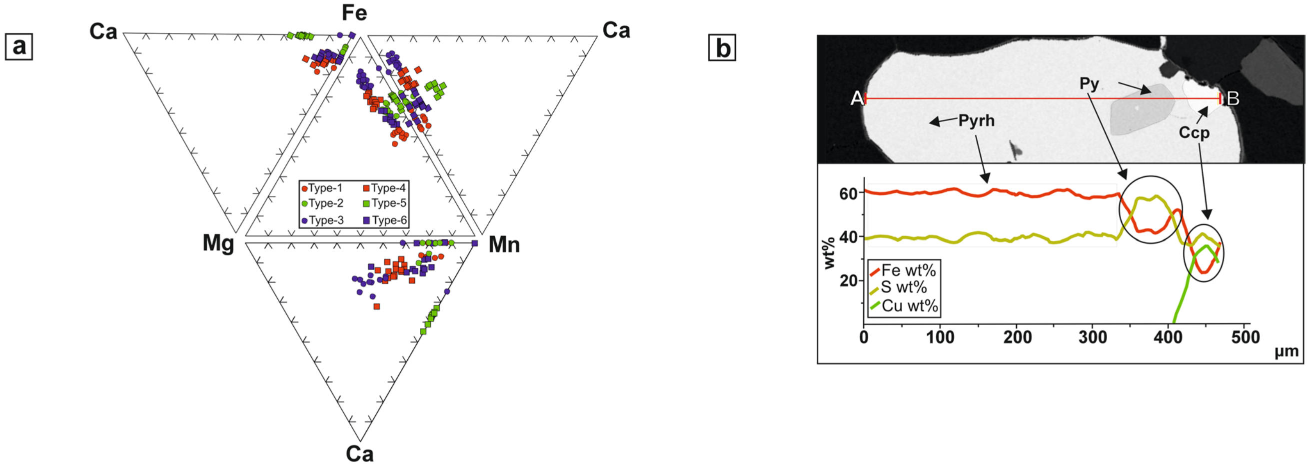

Fig. 6 Major-element distribution diagram of garnet and profile section elemental mapping of sulfide. **a** Ternary compositional diagrams of garnet porphyroblast exhibiting homogenous Fe–Mn rich indicating almandine-spessartine type garnet (modified after Coleman et al. 1965). **b** Profile section analysis of sulfides (pyrrhotite with inclusions of pyrite and chalcopyrite) showing homogenous iron and sulfur distribution (Abbreviations: Py – Pyrite, Pyrh – Pyrrhotite, Ccp – Chalcopyrite)

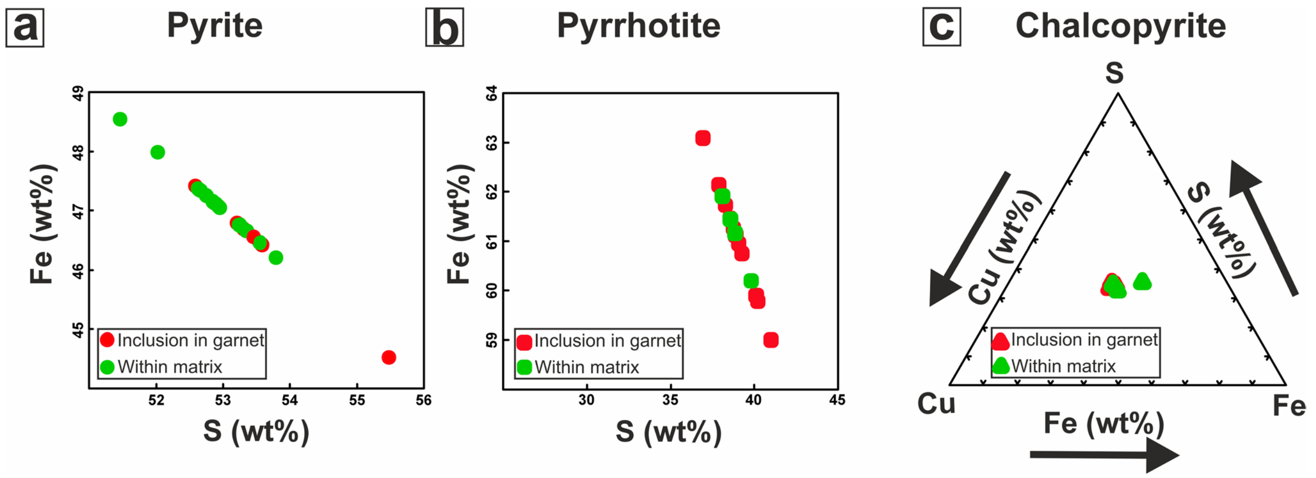

Fig. 7 Major-element distribution of sulfides as inclusions in garnets and within the surrounding matrix based on SEM analysis. **a** X–Y graphical plot of pyrite's iron and sulfur content representing fairly uniform distribution, both for inclusions in garnets and within matrix. **b** X–Y graphical plot of pyrrhotite's iron and sulfur content illustrating moderately homogenous distribution, both for inclusions in garnets and within matrix. **c** Ternary Cu-Fe-S diagram of chalcopyrite showing relatively homogeneous distribution of Fe, Cu and S both for inclusions in garnets and within matrix

supplementary material 3). Separation of quartz, cordierite and feldspar by gray scale intensity was not successful.

3D visualization of garnet porphyroblast displays the spatial distribution of garnets and their microstructures (Fig. 8b; Tables 4–8 in Electronic supplementary material 3). In 3D-rendered images, garnets appear predominantly as clusters embedded in metasedimentary mica-rich layers (Fig. 8a, b; Tables 4, 5 in Electronic supplementary material 3). Two distinct morphologic garnet types are visualized, i.e., sub-rounded to rounded, rotated, sheared garnet type and elongated, folded (often fractured) garnet type (Fig. 8b; Tables 4–8 in Electronic supplementary material 3). The spatial distribution of inclusions in different slices of the 3D-reconstructed images dominantly represents a foliation pattern oriented vertically to the external foliation, indicating syn-kinematic deformation (Fig. 8a). 3D-rendered images display three distinct morphic types of denser minerals (i.e., sulfides and oxides) summarized as elongated, folded types, irregular types and cubic types (Tables 7, 8 in Electronic supplementary material 3). The irregular and elongated, folded types are generally attributed to the sulfide minerals which are visualized from the thin sections study (Fig. 5). However, cubic features are common for both sulfides and oxides (Fig. 5). The penetrative nature of sulfides and oxides is evident in different slices of the 3D images, demonstrated by their pervasive presence throughout the drill core samples (Tables 4–8 in Electronic supplementary material 3). The 3D images reveal that most of the elongated sulfide grains are preferentially localized adjacent to the hinge zone of crenulation cleavages, with grain size increasing in proximity to the hinge zone (Fig. 8a, c; Table 8 in Electronic supplementary material 3). Moreover, most of these minerals follow the S_1 foliation of silicate matrix (Fig. 8a, c). Folded inclusion trails of sulfides are also clearly visible within garnet (Fig. 8a; Tables 4, 7 in Electronic supplementary material 3).

Micro-CT analysis enables us to obtain quantitative measurements (such as volume, surface area, grain size) for sulfide, oxide, and garnet porphyroblast grains in five samples, from which we obtain a successful segmentation of different grains of our interest (Tables 4–10 in Electronic supplementary material 3). The volumetric quantitative analysis indicates that the sulfides and oxides constitute less than 0.5% of the total volume of drill cores, whereas garnet comprises less than 1% of total volume of the whole rock. In addition, the volume fraction of the denser minerals (sulfides and oxides) is less than 1% inside garnets. Garnets from sample PYS-155(A) are cigar-shaped (prolate), whereas garnets from PYS-155(C) are dominantly pancake-shaped (oblate) based on Flinn diagram (Fig. 8d). Moreover, the Flinn diagram for different occurrence of sulfides and oxide grains (i.e., in garnet porphyroblasts and within matrix) illustrates mixtures shapes varying from predominantly prolate to significantly oblate grains (Table 10 in Electronic supplementary material 3). However, sulfides and oxides from sample PYS-129(A) and elongated, folded sulfides from PYS-144(A) are dominantly prolate (Table 10 in Electronic supplementary material 3). We have discarded the sulfide, oxide and garnet grains that intersect the edges or boundaries of the samples due to incomplete access to grain size, axes, and volumetric fractions data for comprehensive analysis. Also, we have excluded quantitative data analysis of grain size smaller than 300 μm to avoid the influence of denser minerals (i.e., zircon).

Discussion

Mixed-state remobilization of sulfides from the Pyhäsalmi deposit halo region in metamorphic environment

During regional metamorphism, massive sulfide deposits can undergo intense metamorphism and deformation, leading to significant modifications in their shape, spatial distribution, mineral assemblages, and ore fabric (Vokes 1969; Barnes 1987; Cook et al. 1993; Marshall and Gilligan 1993; Zhang et al. 2014a, b; Zhong et al. 2015). Hence, metamorphism accompanying deformation often naturally promotes ore deposit remobilization. Correspondingly, the sulfides in the Paleoproterozoic Pyhäsalmi deposit halo region are deformed and remobilized, which is evidenced by their prominent elongated, folded and foliated textures along with compositional homogeneity (Figs. 5, 7, 8). Metamorphic remobilization that involves the translocation of preexisting mineralization occurs either by solid-state (mechanical), liquid-state (chemical), and/or mixed-state transfer processes (Larocque and Hodgson 1995; Marshall et al. 2000; Andersson et al. 2016). Mechanical remobilization of massive sulfides typically results in limited local redistribution, whereas chemical remobilization facilitates more extensive external redistribution, often leading to the formation of new mineralization sites (Vokes 1969; Cox et al. 1981; Marshall and Gillian 1987; Zheng et al. 2012).

The sulfides in the Pyhäsalmi region, particularly the two dominant phases pyrite and pyrrhotite from the halo region, were remobilized through a combination of solid-state (mechanical) and liquid-state (chemical) transfer processes, highlighting the mixed-state remobilization characteristic of the region. Mechanical remobilization includes the translocation of sulfides by cataclastic flow, dislocation flow and diffusive mass transfer and is determined by the competence of the minerals. The presence of elongated ductile pyrite crystals from the Pyhäsalmi region can be attributed to the product of deformation accompanying recrystallization at high-grade metamorphism (Fig. 5a, h). Pyrite, as a brittle sulfide and isometric mineral, shows elongation that reflects a history of dislocation flow and recrystallization under directed pressure during metamorphism (Vokes 1969; Cox et al. 1981; Barrie et al. 2007, 2010). Moreover, some of the pyrites have been subjected to cataclastic deformation, which is observed by the presence of brecciated-granular, occasionally fractured grains (Fig. 5a). Similarly, the ductile behavior of pyrrhotite, evident in its elongated, folded, and foliated morphology, supports metamorphic remobilization (Fig. 5d–h). The flattening of folded and foliated sphalerite in the Pyhäsalmi region further indicates mechanical remobilization (Fig. 5h). Further, the presence of durchbewegung texture illustrates dislocation flow and rotational movement of competent ore minerals (such as pyrite) within an incompetent, ductile sulfide matrix (such as pyrrhotite) (Vokes 1969; Plimer 1984; Marshall and Gillian 1989; Zheng et al. 2016). This texture indicates dynamic recrystallization during shearing and folding, reflecting mechanical migration (Vokes 1969; Maiden et al. 1986; Marshall and Gillian 1989; Zhang et al. 2014a, b). These morphological features of the dominant sulfides in the Pyhäsalmi region predominantly suggest mechanical remobilization in metamorphic environments. Additionally, the tendency of Pyhäsalmi sulfides to be

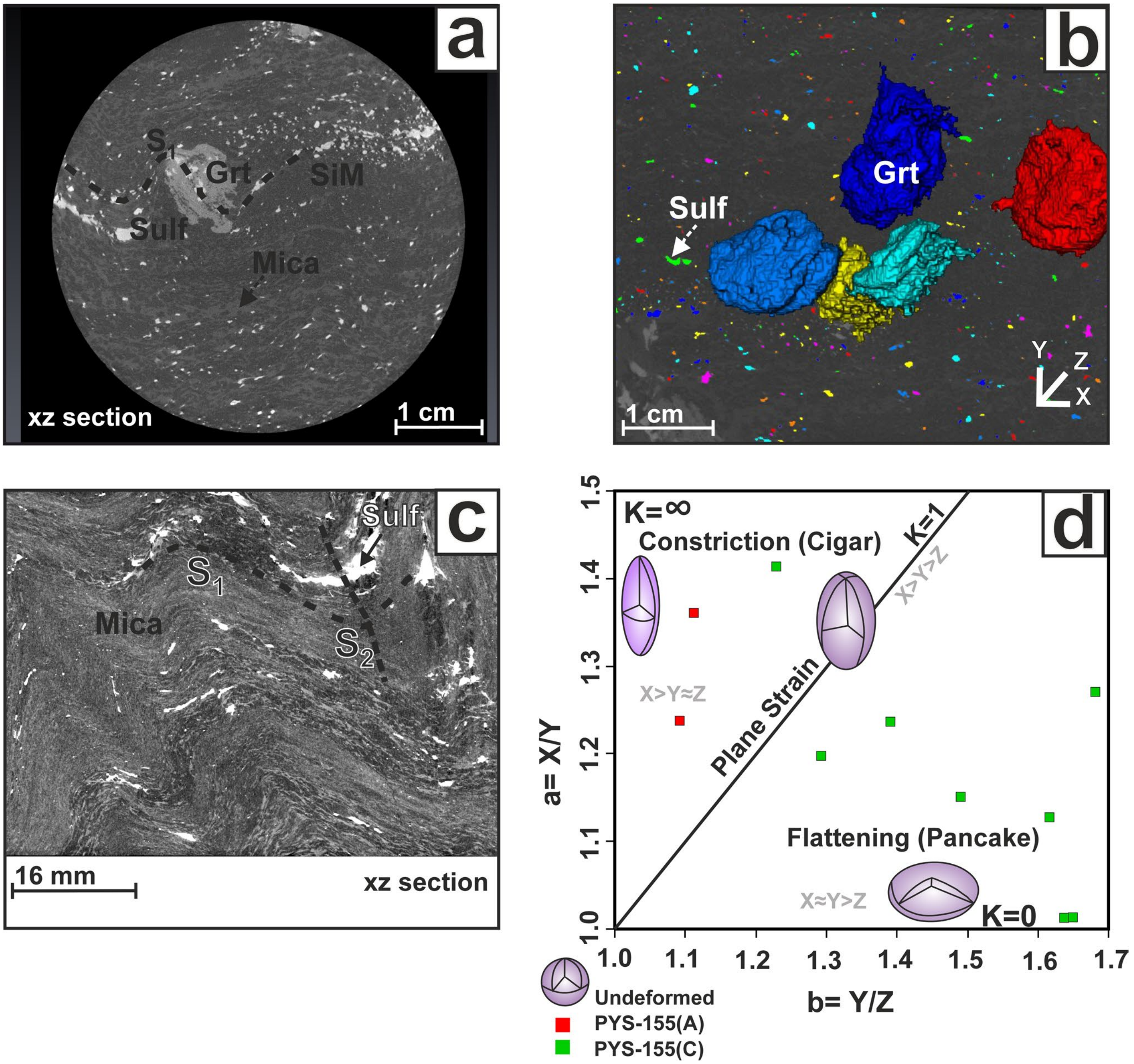

Fig. 8 3D rock fabric analysis using Micro-CT. **a** XZ section of a 3D-rendered gray scale image from sample PYS-155(B) illustrates segmentation of denser mineral assemblages (brightest region) and less dense mineral assemblages (darker region). The brightest region is attributed to sulfide grains, followed by garnet porphyroblast, whereas the darker region is attributed to mica, followed by silica-rich matrix (i.e., quartz-feldspar-cordierite matrix). The inclusion pattern within the garnet follows continuity of external S_1 foliation, which reveals syn-kinematic growth of the garnet. **b** Snapshot of a 3D-rendered image from sample PYS-155(B) exhibits the spatial distribution of garnets, sulfides and oxide grains. Two different morphic garnet porphyroblasts, i.e., rounded rotated type (red color) and elongated type (blue and yellow color) are visualized. The color coding used in this image for the sulfide and oxide grains does not imply any special attributes. **c** XZ section of a 3D-rendered gray scale image from sample PYS-144(B) shows crenulation cleavages. The elongated, folded sulfides are mostly spatially distributed in the hinge region of the crenulation cleavages and dominantly follow the S_1 foliation. The sulfides also portray a tendency to increase in size proximal to the hinge zone. **d** The Flinn diagram illustrates that garnets from PYS-155(A) are cigar-shaped (prolate), whereas garnets from PYS-155(C) represent dominantly pancake-shaped (oblate) (Abbreviations: Sulf – Sulfide, Grt – Garnet, SiM – Silicate matrix)

thicker in fold hinges highlights dislocation characteristics of remobilized sulfides (Fig. 8c). The penetrative nature of sulfides and their homogeneous composition (i.e., consistent iron and sulfur content across different sulfide types) further indicates dominant mechanical remobilization (Fig. 7; Table 3 in Electronic supplementary material 3). Recrystallization and the spatial distribution of disseminated pyrrhotite along the grain boundaries of silicates (e.g., garnet, biotite, and quartz) suggest plastic flowage facilitated by fluid activity, indicative of liquid-state remobilization (Fig. 8). Liquid-state chemical remobilization is achieved through coupled-dissolution-reprecipitation (CDR) mechanism, which entails the redistribution of minerals as a dissolved liquid phase originating from diverse sources, such as circulating meteoric or seawater, metamorphic dewatering fluids, magma, and sulfide anatectic melts (Marshall et al. 2000; Putnis 2002, 2009). Moreover, the transport of minerals through chemical remobilization frequently results in veinlets and mineralization within strain shadows (Andersson et al. 2016). In the Pyhäsalmi deposit, pyrite, pyrrhotite, and chalcopyrite also occur as fracture-filling veinlets within garnet and cordierite (Fig. 5c, e), further supporting fluid-influenced remobilization. The spatial distribution of pyrrhotite in the schistose rocks along microfold hinges demonstrates fluid transfer activity, which created preferential sites for mineral deposition (Fig. 8a, c).

Polyphase remobilization events of Pyhäsalmi sulfides

Based on petrographic, SEM–EDS and micro-CT analysis, our study illustrates at least two stages of sulfide remobilization events from the Pyhäsalmi deposit halo region. This supports the study by Laine et al. (2015) that emphasizes two-stage remobilization events of the Pyhäsalmi massive ore, corresponding to the deformational phases (Fig. 9). The first remobilization event of Pyhäsalmi sulfides portrays dominant mechanical (solid-state) processes represented by penetrative, elongated, foliated and cubic sulfides (Figs. 5a, b, d-e, 9a), with limited pressure solution evidenced by rounded corners of cubic sulfides. The cubic type sulfides (*Pyrite 2* and *Pyrrhotite 2*) may reflect syn-D_1-D_2 phase growth, demonstrated by their broken and rounded corners representing mechanical abrasion and occasionally pressure solution (McClay and Ellis 1984; Cox 1987; Fig. 5a, d). The sub-rounded and elongated sulfides (*Pyrite 1* and *Pyrrhotite 1*) probably formed during the late stage of the D_1-D_2 phase which probably facilitated the plastic flow of the sulfides. The elongated sulfides typically follow S_1 foliation in mica-rich matrix and occasionally in garnet porphyroblast (Figs. 4, 5b, e, 9a). This mechanically remobilized, elongated and foliated pyrite and pyrrhotite inclusions in garnet Type-6 (almandine) suggest that the first remobilization event started before the peak metamorphic conditions (600–650 °C/4–5 kbar) in the Pyhäsalmi region (Figs. 4f, 9b-c). Moreover, inclusions of staurolite, cordierite, and biotite in the garnet Type-6 are likely part of the same medium to high temperature–pressure peak metamorphic condition (Figs. 4f, 9c). This initial remobilization event, represented by mineralogical evidences in the Pyhäsalmi region, occurred during the D_1-D_2 phase of the first compressional stage (1.91 Ga) characterized by the collision of the older Svecofennian volcanic arc with the Archean basement, as proposed by Laine et al. 2015 (Fig. 9c; Huhtala 1979; Ekdahl 1993; Roberts et al. 2003). The Flinn diagram shows the presence of distinct, oblate, pancake-shaped sulfides, which suggests a flattening-type of deformation attributed to this geodynamic collisional regional event (Table 10 in Electronic supplementary material 3).

The later and final remobilization event of Pyhäsalmi sulfides reflects a mixed-state (physical and chemical) remobilization process, as evidenced by folded, fractured, cataclastic, and fracture-filling vein-type sulfides, such as pyrite, pyrrhotite, and chalcopyrite (Figs. 5a, c, d, f, h, 9a). The intense shearing and compression of the D_4 phase accounts for brittle-ductile behavior characterized by cataclastic and folded grains, demonstrated predominantly by *Pyrite 3* and *Pyrrhotite 3* (Figs. 5a, h, 9a). Spatial distribution of sulfide minerals often shows attenuation to the hinge zone of crenulation cleavages due to D_4 shearing, with a tendency for increased sulfide grain size at hinge areas (Figs. 8c, 9a). Moreover, the durchbewegung texture represents dynamic recrystallization during the D_4 shearing. Sulfides associated with this remobilization event are frequently observed as inclusions inside the cataclastic garnets (garnet Type-1), the syn-kinematic garnets (garnet Type-4), and the rotated deformed garnets (garnet Type-3) (Figs. 4a, c, d, 9c). This second remobilization event is correlated to the second metamorphic peak condition denoted by Fe–Mn-Ca-rich garnets, cordierite, sillimanite and mica, indicating a higher temperature–pressure condition (possibly 650–700° C/4–7 kbar) than the first event based on the occurrence of sillimanite (Figs. 4a, c, d, 9c). However, this well evidenced mixed-state second stage remobilization event must have persisted to the following relatively lower temperature retrograde metamorphic conditions (ca. 350–500 °C) demonstrated by late-stage fracture filling of chalcopyrite and fractured pyrite (Figs. 5c, 9a) (Cox et al. 1981; Marshall and Gillian 1993; Barrie et al. 2009, 2010). Laine et al. (2015) proposed a second-stage remobilization event for Pyhäsalmi sulfides during the second compressional stage (D_4 phase, 1.82–1.79 Ga). This event is characterized by a shift in the compression direction to N-S, the formation of basin-dome structures, refolding of earlier D_3 folds, and intense shearing within the horsetail system of the OjSZ shear zone (Figs. 1, 9b; Ekdahl 1993; Roberts et al 2003). The Flinn diagram reveals the presence of distinct prolate, cigar-shaped sulfides, which suggests a constriction-type of deformation attributed to this dynamothermal geodynamic regional event (Table 10 in Electronic supplementary material 3).

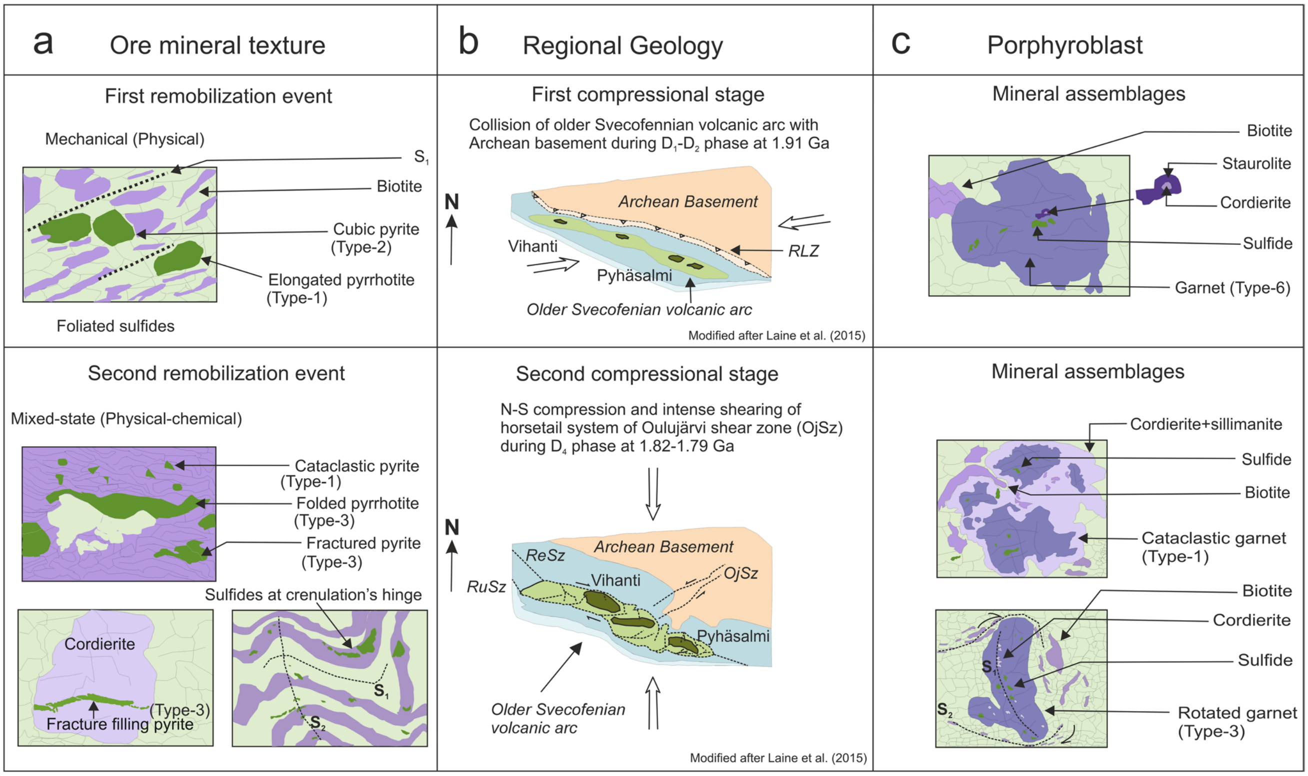

Fig. 9 The schematic diagram illustrating Pyhäsalmi sulfide remobilization processes during polyphase deformational phases. **a** The ore minerals underwent two stages of remobilization. The initial remobilization event was dominated by solid-state transfer processes, as evidenced by foliated, elongated, and cubic ore minerals. The final remobilization event was characterized by mixed-state processes, indicated by cataclastic textures, folded and fracture-filling sulfides, as well as the spatial distribution tendency of sulfides within the hinge zone of crenulation cleavages. **b** The regional deformational history of the Vihanti-Pyhäsalmi region corresponding to the two remobilization events which suggests the collision of older Svecofennian island arc with the Archean basement during D_1-D_2 collisional deformational phases at 1.91 Ga facilitate the initial mechanical remobilization of the sulfides and the intense shearing of Oulujärvi horsetail shear system as well as N-S compression during the D_4 collisional phase resulted in mixed-state remobilization for the sulfide minerals (modified after Laine et al. 2015). (Abbreviations: RLZ = Raahe-Ladoga shear zone, OjSz = Oulujärvi shear zone, ReSz = Revonneva shear zone, and RuSz = Ruhaperä shear zone) **c** The metamorphic mineral assemblage of garnet, cordierite and staurolite represents the metamorphic conditions during the initial dominant solid-state transfer processes, whereas garnet, sillimanite and cordierite portray metamorphic conditions during the final mixed-state remobilization event

Metamorphic conditions of remobilized sulfides from the Pyhäsalmi deposit halo region

Studies show that sulfide remobilization (i.e., mechanical and chemical remobilization) is enhanced with increasing temperature (Zheng et al. 2012). Sulfide assemblages, especially found in stable silicate minerals (such as garnet), are pivotal in studying their peak metamorphic conditions. In contrast, sulfides in the rock matrix are open to influence by later fluid activity, which results in alteration and transformation of the original products. Remobilized pyrite from the Pyhäsalmi halo region releases sulfur during prograde metamorphism, corresponding to increasing temperature. This pyrite de-sulfidation and later binding of the metal iron from wall rocks leads to the formation of pyrrhotite (Fig. 5b; Table 2 in Electronic supplementary material 3) during amphibolite facies conditions. The reaction can be represented as follows (Tomkins 2007):

$$3\ \mathrm{FeS}_{2(\mathrm{pyrite})} + 2\mathrm{H_2O} \rightarrow 3\mathrm{FeS}_{(\mathrm{pyrrhotite})} + 2\mathrm{H_2S} + \mathrm{SO_2} \tag{1}$$

$$\mathrm{H_2S} + \text{Fe-Mg amphibole} + \tfrac{1}{2}\,\mathrm{O_2} \rightarrow \mathrm{FeS} + \text{Mg-amphibole} + \mathrm{H_2O} \tag{2}$$

The common coexistence of pyrite and pyrrhotite from the studied region indicates an equilibrium temperature above 300° C (e.g., Fig. 5g) (Marshall and Gillian 1987). The plastic behavior of Pyhäsalmi pyrite (Pyrite 1 and 3) reveals recrystallization occurred at 550–650° C, whereas the brittle behavior of Pyrite 2 implies the effect of post-peak metamorphic conditions below 500 °C (Boyle et al. 1998; Freitag et al. 2004; Barrie et al. 2007, 2010). Typical pressure–temperature range for sulfide remobilization under regional metamorphic conditions has been estimated at 200–700 °C and 20–100 MPa (Hank and Raleigh 1980; Turner 1981; Gillian and Marshall 1987). The most dominant sulfide mineral occurring as inclusions inside garnet is pyrite. Additionally, sulfide assemblages such as pyrite + pyrrhotite, pyrite + chalcopyrite, and pyrite + chalcopyrite are also present as inclusions (Table 2 in Electronic supplementary material 3). This implies that polymetallic hydrothermal fluid was present before the peak of metamorphism. On the other hand, similar sulfide mineral assemblages such as pyrite + pyrrhotite, pyrite + pyrrhotite + chalcopyrite and notably sphalerite + chalcopyrite + pyrrhotite, are also present in the matrix (Fig. 5). Garnet porphyroblast generally imposes a barrier for its sulfide inclusions to prevent communication to the external conditions (i.e., external fluids activity), which results in the creation of a closed system for the sulfide inclusions (Putnis 2002, 2009; Tomkins 2007). However, the presence of fractures and cracks inside the garnets can serve as conduits for fluid transportation between the inclusions and the matrix (Fig. 8) (Putnis 2002, 2009; Kawakami et al. 2006). The garnets from the Pyhäsalmi region have visible fractures connecting sulfide inclusions and matrix (Fig. 4f), which can be attributed to the absence of distinct sulfide mineral assemblages in the matrix and garnets. This implies similar fluid activity during metamorphic events, which can be the probable reason for nearly homogenous compositional distribution of sulfides in groundmasses and inside garnets (Fig. 6b). In addition, the coexistence of euhedral cubic idiomorphic magnetite with chlorite, pyrite, and quartz minerals indicates they were formed by hydrothermal fluids in the study region (Fig. 5i) (Maghfouri et al. 2021). Moreover, the magnetite often shows low content of Ti and V along with intergrowth of ilmenite, representing low temperature hydrothermal fluid activities (Dupuis and Beaudoin 2011; Maghfouri et al. 2021). The mineral assemblages, i.e., garnet + staurolite + cordierite + biotite, garnet + cordierite + sillimanite + biotite, garnet + cordierite + anthophyllite + biotite of the Pyhäsalmi halo region emphasize that the region has been metamorphosed in amphibolite facies conditions (Fig. 4). The highest metamorphic grade achieved by this region is the sillimanite zone, which points to constraints of 650–700 °C as the upper temperature limit for the studied region (Fig. 4a, b; Zhou et al. 2023). However, extensive chloritization of mica (i.e., biotite and muscovite), sillimanite, anthophyllite, garnet and epidotization of plagioclase and biotite indicate late-stage retrograde metamorphic fluid activity in that region (Fig. 3). The local shear zone of this region possibly provides a conduit for hydrothermal fluid transportation (Fig. 1).

Decoding the regional deformation history—insights from microstructural analysis

The Pyhäsalmi region has undergone two major deformational stages: (a) the first compressional stage with three phases (D_1, D_2, D_3) and (b) the last compressional stage with a single phase (D_4; Ekdahl 1993; Laine et al. 2015). Combining the 3D visualization of porphyroblast (i.e., shape, orientation, inclusions and spatial distribution) with 2D petrographic study unravels the porphyroblast growth history relative to these deformational phases. The study of inclusion patterns in porphyroblasts relative to matrix foliation, especially in three-dimensional space, enhances the ability to detect detailed information and define multiple deformational phases that can be implicated in regional deformational history. The D_1-D_2 phase represents the collision of the older Svecofennian volcanic with the Archean basement in the Fennoscandian Shield, demonstrated by granoblastic texture (quartz-biotite), nematoblastic texture (anthophyllite-fibrolite), garnet types 2 and 6, as well as formation of penetrative S_1 foliation (Figs. 3, 4c, f, 9). Well preserved S_1 inclusion trails of elongated sulfide and silicate in garnet porphyroblasts are characteristics of the D_1-D_2 deformational phase (Fig. 8a). In addition, 3D visualization of elongated oblate sulfides illustrates the parallel alignment of the grains along the penetrative S_1 foliation, which indicates syn-D_1-D_2 phase growth of these sulfides (Figs. 8a, 9). Folding, stretching of the D_3 phase causes fracturing and overgrowth of garnet (Type-6), kinking of biotite, as well as formation of stretched quartz (Fig. 4b, c, f). The Flinn diagram exhibits the presence of distinct oblate pancake-shaped garnet porphyroblasts and sulfides, suggesting a flattening-type deformation attributed to this first collisional event in the Pyhäsalmi region (Fig. 8d). The second compressional stage (D_4) of this region is marked by intense shearing, which is demonstrated by rotated elongated garnet porphyroblasts (Type-3), cataclastic garnet (Type-1), and formation of crenulation cleavages (Fig. 4a, c, d). The D_4 phase causes ductile deformation of the garnets, which results in bending of the porphyroblast (Figs. 4c, 8b, 9). During this phase, elongated garnet porphyroblasts grow preferentially on the limbs of crenulation cleavages, while sulfide exhibits zonation along the hinge zones (Figs. 8c, 9; Table 5 in Electronic supplementary material 3). The crenulation cleavages with penetrative S_1 and S_2 foliation reflect the refolding of the previous folds during the D_4 phase, recording the progressive deformation history. The Flinn diagram portrays the presence of distinct prolate shape garnet porphyroblasts, illustrating a constriction-type deformation associated with shearing of the Oulujärvi shear zone during the D_4 phase deformation in the Pyhäsalmi region (Fig. 8d).

Conclusions

By integrating metamorphic mineral assemblages and microstructural analysis, our study presents a framework for constraining multistage ore mineral remobilization events in polyphase deformational and metamorphic environments from the Paleoproterozoic bimodal Pyhäsalmi VMS deposit halo in the Fennoscandian Shield. The following conclusions are inferred from this study:

1. The sulfides from the halo region have undergone mixed-state remobilization: (a) The solid-state (mechanical) remobilization is evidenced by cataclastic flow of brecciated pyrite and pyrrhotite, fractured pyrite, flattened, foliated and folded sulfide. (b) The liquid-state remobilization is indicated by the spatial distribution of disseminated pyrrhotite around the grain boundaries of silicate porphyroblasts, fracture filling (pyrite, pyrrhotite, and chalcopyrite), and the hinge zone concentration of sulfides (pyrite, pyrrhotite) in crenulation cleavages.
2. We have identified two distinct remobilization events: (a) The first stage, associated with D_1-D_2 phase, is dominated by solid-state remobilization processes that possibly occurred before the metamorphic peak denoted by staurolite + garnet + cordierite, and (b) The second stage, linked to D_4 phase, is characterized by mixed-state remobilization processes that possibly occurred during metamorphic peak conditions represented by sillimanite + garnet + cordierite + biotite.
3. The metamorphic mineral assemblages from the Pyhäsalmi suggest upper amphibolite facies conditions (650–700 °C), as indicated by the presence of sillimanite + garnet + cordierite + biotite. The plastic deformation of the Pyhäsalmi pyrite indicates recrystallization at 550–650 °C, whereas the brittle behavior of the pyrite suggests post-peak metamorphic conditions below 500 °C.
4. The oblate pancake-shaped garnet porphyroblasts and sulfides in the Flinn diagram suggest a flattening-type deformation which is attributed to the D_1-D_3 deformational phase in the Pyhäsalmi region, whereas the prolate cigar-shaped garnet porphyroblasts and sulfides in the Flinn diagram illustrate constriction-type deformation which is associated with intense shearing of the Oulujärvi shear zone during the D_4 deformational phase.

Supplementary Information The online version contains supplementary material available at https://doi.org/10.1007/s00531-025-02511-4.

Acknowledgements We are grateful to the K.H. Renlund foundation (K.H. Renlunds Stiftelse) for providing financial support. We thank Arto Peltola from the University of Turku and Sören Fröjdö from Åbo Akademi University for thin section preparation and imaging. We thank Jani Jäsperi from the Geological Survey of Finland for providing drill core data. We acknowledge the Materials Research Infrastructure (MARI) at the Department of Physics and Astronomy, University of Turku for access and support with the SEM facilities. Micro-CT was funded by the Research Council of Finland via the RAMI infrastructure project (#293109). We like to express gratitude for the editorial handling by Ulrich Riller and constructive reviews by Stephanie Bruckner and an anonymous reviewer.

Funding Open Access funding provided by University of Turku (including Turku University Central Hospital). This research, a part of doctoral thesis, is funded by K.H. Renlund foundation (K.H. Renlunds Stiftelse) and conducted at the University of Turku.

Data availability All the data supporting this research are available in this paper and in the supplementary materials.

Declarations

Conflict of interest The authors declare that they have no known competing financial interests or personal relationships that could have appeared to influence the work reported in this paper.

References

Andersson SS, Jonsson E, Högdahl K (2016) Metamorphism and deformation of a Palaeoproterozoic polymetallic sulphide–oxide mineralisation: Hornkullen, Bergslagen, Sweden. GFF 138:410–423. https://doi.org/10.1080/11035897.2015.1135187

Baker DR, Mancini L, Polacci M, Higgins MD, Gualda GAR, Hill RJ, Rivers ML (2012) An introduction to the application of X-ray microtomography to the three-dimensional study of igneous rocks. Lithos 148:262–276. https://doi.org/10.1016/j.lithos.2012.06.008

Barnes RG (1987) Multi-stage mobilization and remobilization of mineralization in the broken hill block, Australia. Ore Geol Rev 2:247–267. https://doi.org/10.1016/0169-1368(87)90031-X

Barrie CD, Boyle AP, Prior DJ (2007) An analysis of the microstructures developed in experimentally deformed polycrystalline pyrite and minor sulphide phases using electron backscatter diffraction. J Struct Geol 29:1494–1511. https://doi.org/10.1016/j.jsg.2007.05.005

Barrie CD, Boyle AP, Salter M (2009) How low can you go?—Extending downwards the limits of plastic deformation in pyrite. Mineral Mag 73:895–913. https://doi.org/10.1180/minmag.2009.073.6.895

Barrie CD, Cook NJ, Boyle AP (2010) Textural variation in the pyrite-rich ore deposits of the Røros district, Trondheim Region, Norway: implications for pyrite deformation mechanisms. Miner Deposita 45:51–68. https://doi.org/10.1007/s00126-009-0261-3

Bell TH, Johnson SE (1989) Porphyroblast inclusion trails: the key to orogenesis. J Metamorph Geol 7:279–310. https://doi.org/10.1111/j.1525-1314.1989.tb00598.x

Boyle AP, Prior DJ, Banham MH, Timms NE (1998) Plastic deformation of metamorphic pyrite: new evidence from electron-backscatter diffraction and forescatter orientation-contrast imaging. Mineral Deposita 34:71–81. https://doi.org/10.1007/s001260050186

Cartwright I, Oliver NHS (1998) Metamorphic Fluids and their Relationship to the Formation of Metamorphosed and Metamorphogenic Ore Deposits. In: Vokes FM, Marshall B, Spry PG (eds) Metamorphic and Metamorphogenic Ore Deposits. Rev Econ Geol 11:81–96. https://doi.org/10.5382/Rev.11.04

Castroviejo R, Quesada C, Soler M (2011) Post-depositional tectonic modification of VMS deposits in Iberia and its economic significance. Miner Deposita 46:615–637. https://doi.org/10.1007/s00126-010-0306-7

Cloutier J, Piercey SJ, Layne G et al (2015) Styles, textural evolution, and sulfur isotope systematics of Cu-rich sulfides from the Cambrian whalesback volcanogenic massive sulfide deposit, Central Newfoundland, Canada. Econ Geol 110:1215–1234. https://doi.org/10.2113/econgeo.110.5.1215

Coleman RG, Lee DE, Beatty LB, Brannock WW (1965) Eclogites and Eclogites: their differences and similarities. Geol Soc Am Bull 76:483–508

Cook NJ, Halls C, Boyle AP (1993) Deformation and metamorphism of massive sulphides at Sulitjelma, Norway. Mineral Mag 57:67–81. https://doi.org/10.1180/minmag.1993.057.386.07

Corti L, Zucali M, Visalli R, Mancini L, Sayab M (2019) Integrating X-ray computed tomography with chemical imaging to quantify mineral re-crystallization from granulite to eclogite metamorphism in the western Italian Alps (Sesia-Lanzo Zone). Front Earth Sci Vol 7:327. https://doi.org/10.3389/feart.2019.00327

Cox SF (1987) Flow mechanisms in sulphide minerals. Ore Geol Rev 2:133–171. https://doi.org/10.1016/0169-1368(87)90026-6

Cox SF, Etheridge MA, Hobbs BE (1981) The experimental ductile deformation of polycrystalline and single crystal pyrite. Econ Geol 76:2105–2117. https://doi.org/10.2113/gsecongeo.76.8.2105

Dempster TJ, La Piazza J, Taylor AG et al (2017) Chemical and textural equilibration of garnet during amphibolite facies metamorphism: the influence of coupled dissolution–reprecipitation. J Metamorph Geol 35:1111–1130. https://doi.org/10.1111/jmg.12278

Denison C, Carlson WD, Ketcham RA (1997) Three-dimensional quantitative textural analysis of metamorphic rocks using high-resolution computed X-ray tomography: part I. Methods and techniques. J Metamorph Geol 15:29–44. https://doi.org/10.1111/j.1525-1314.1997.00006.x

Dupuis C, Beaudoin G (2011) Discriminant diagrams for iron oxide trace element fingerprinting of mineral deposit types. Miner Deposita 46:319–335. https://doi.org/10.1007/s00126-011-0334-y

Duuring P, Hassan L, Zelic M, Gessner K (2016) Geochemical and spectral footprint of metamorphosed and deformed VMS-style mineralization in the Quinns District, Yilgarn Craton, Western Australia. Econ Geol 111:1411–1438. https://doi.org/10.2113/econgeo.111.6.1411

Ekdahl E (1993) Early Proterozoic Karelian and Svecofennian formations and the evolution of the Raahe-Ladoga ore zone, based on the Pielavesi area, Central Finland. Geol Surv Finland Bull 373:137

Etheridge MA, Wall VJ, Cox SF, Vernon RH (1984) High fluid pressures during regional metamorphism and deformation: implications for mass transport and deformation mechanisms. J Geophys Res Solid Earth 89:4344–4358. https://doi.org/10.1029/JB089iB06p04344

Ferré EC, Gébelin A, Till JL, Sassier C, Burmeister KC (2014) Deformation and magnetic fabrics in ductile shear zones: a review. Tectonophysics 629:179–188. https://doi.org/10.1016/j.tecto.2014.04.008

Franklin JM, Gibson HL, Jonasson IR, Galley AG (2005) Volcanogenic massive sulfide deposits. In: Hedenquist JW, Thompson JFH, Goldfarb RJ, Richards JP (eds) One Hundredth Anniversary Volume. The Economic Geology Publishing Company, pp 523–560

Franklin JM (1993) Volcanic-associated massive sulphide deposits. In: Kirkham RV, Sinclair WD, Thorpe RI, Duke JM (eds) Mineral deposit modeling. Geological Association of Canada, Special Paper 40:315–334

Franklin JM (1996) Volcanic-associated massive sulphide base metals. In: Eckstrand OR, Sinclair WD, Thorpe RI (eds) Geology of Canadian mineral deposit types. Geological Survey of Canada, Geology of Canada 8:158–183

Freitag K, Boyle AP, Nelson E et al (2004) The use of electron backscatter diffraction and orientation contrast imaging as tools for sulphide textural studies: example from the Greens Creek deposit (Alaska). Miner Deposita 39:103–113. https://doi.org/10.1007/s00126-003-0386-8

Gaál G, Gorbatschev R (1987) An outline of the precambrian evolution of the baltic shield. Precambr Res 35:15–52. https://doi.org/10.1016/0301-9268(87)90044-1

Galley AG, Hannington MD, Jonasson IR (2007) Volcanogenic massive sulphide deposits. Geological Association of Canada, Mineral Deposits Division, pp 141–161

Gu L, McClay K (1992) Pyrite deformation in stratiform lead-zinc deposits of the Canadian Cordillera. Miner Deposita 27:169–181. https://doi.org/10.1007/BF00202540

Hanks TC, Raleigh CB (1980) The conference on magnitude of deviatoric stresses in the earth's crust and uppermost mantle. J Geophys Res 85:6083–6085. https://doi.org/10.1029/JB085iB11p06083

Hannington MD (2014) Volcanogenic massive sulfide deposits. In: Holland HD, Turekian KK (eds) Treatise on geochemistry, 2nd edn. Elsevier, Oxford, pp 463–488

Heinonen S (2013) Seismic reflection profiling for massive sulfide exploration in Finland. Dissertation, University of Helsinki

Helovuori O (1979) Geology of the Pyhäsalmi ore deposit, Finland. Econ Geol 74:1084–1101. https://doi.org/10.2113/gsecongeo.74.5.1084

Hölttä P (1988) Metamorphic zones and the evolution of granulite grade metamorphism in the early Proterozoic Pielavesi area, central Finland. Geol Surv Finland Bull 344:1–50

Huhtala T (1979) The geology and zinc-copper deposits of the Pyhasalmi-Pielavesi District, Finland. Econ Geol 74:1069–1083. https://doi.org/10.2113/gsecongeo.74.5.1069

Imaña M (2003) Petrography, Mineralogy, Geochemistry and 3D Modelling of the A Zinc ore in the Pyhasalmi Zn-Cu VMS deposit, central Finland. Dissertation, University of Turku

Johnson SE (1999) Porphyroblast microstructures: a review of current and future trends. Am Miner 84:1711–1726. https://doi.org/10.2138/am-1999-11-1202

Kärki A, Laajoki K, Luukas J (1993) Major Palaeoproterozoic shear zones of the central Fennoscandian Shield. Precambr Res 64:207–223. https://doi.org/10.1016/0301-9268(93)90077-F

Kawakami T, Ellis DJ, Christy AG (2006) Sulfide evolution in high-temperature to ultrahigh-temperature metamorphic rocks from Lützow-Holm Complex, East Antarctica. Lithos 92:431–446. https://doi.org/10.1016/j.lithos.2006.03.057

Ketcham RA (2005) Three-dimensional grain fabric measurements using high-resolution X-ray computed tomography. J Struct Geol 27:1217–1228. https://doi.org/10.1016/j.jsg.2005.02.006

Ketcham RA, Carlson WD (2001) Acquisition, optimization and interpretation of X-ray computed tomographic imagery: applications to the geosciences. Comput Geosci 27:381–400. https://doi.org/10.1016/S0098-3004(00)00116-3

Ketcham RA, Slottke DT, Sharp JM Jr (2010) Three-dimensional measurement of fractures in heterogeneous materials using high-resolution X-ray computed tomography. Geosphere 6:499–514. https://doi.org/10.1130/GES00552.1

Knipe RJ (1989) Deformation mechanisms—recognition from natural tectonites. J Struct Geol 11:127–146. https://doi.org/10.1016/0191-8141(89)90039-4

Korsman K, Hölttä P, Hautala T, Wasenius P (1984) Metamorphism as indicator of evolution and structure of the crust in eastern Finland: Geological Survey of Finland, Bulletin 328:1–40

Korsman K, Niemela R, Wasenius P (1988) Multistage evolution of the Proterozoic crust in the Savo schist belt, eastern Finland. Geol Surv Finland Bull 343:89–96

Korsman K, Koistinen T, Kohonen J et al (1997) Suomen kallioperäkartta—Berggrundskarta över Finland—Bedrock map of Finland 1:1,000,000. Geological Survey of Finland, Espoo, Finland

Korja T, Luosto U, Korsman K, Pajunen M (1994) Geophysical and metamorphic features of Paleoproterozoic Svecofennian orogeny and Palaeoproterozoic overprinting on Archaean crust. Geol Surv Finland Guide 37:11–20

Kousa J, Luukas J, Huhma H, Mänttäri I (2013) Palaeoproterozoic 1.93–1.92 Ga Svecofennian rock units in the northwestern part of the Raahe-Ladoga zone, Central Finland. Report of Investigation Geol Surv Finland 198:91–96

Kousa J, Marttila E, Vaasjoki M (1994) Petrology, geochemistry and dating of Paleoproterozoic metavolcanic rocks in the Pyhajarvi area, central Finland. Special Paper Geol Surv Finland 19:7–27

Lahtinen R (1994) Crustal evolution of the Svecofennian and Karelian domains during 2.1–1.79 Ga, with special emphasis on the geochemistry and origin of 1.93–1.91 Ga gneissic tonalites and associated supracrustal rocks in the Rautalampi area, central Finland. Geological Survey of Finland Bulletin 378:130

Laitala J (2015) Mineralogy and geochemistry of the pyrrhotite horizons in the Pyhäsalmi district, central Finland. Dissertation, University of Turku

Laitala J (2016) Pyrrhotite horizons of the Pyhäsalmi District, Central Finland. In: André-Mayer A-S, Cathelineau M, Muchez P, Pirard E, Sindern S (eds) Mineral resources in a sustainable world, 13th SGA biennial meeting 2015. Proceedings, Vol 5: 2067

Laine E, Luukas J, Mäki T, Kousa J, Ruotsalainen A (2015) The Vihanti-Pyhäsalmi Area. In: Weihed P (ed) 3D, 4D and predictive modelling of major mineral belts in Europe. Springer International Publishing, Cham, pp 123–144

Large RR (1992) Australian volcanic-hosted massive sulfide deposits; features, styles, and genetic models. Econ Geol 87:471–510

Larocque ACL, Hodgson CJ (1995) Effects of greenschist-facies metamorphism and related deformation on the Mobrun massive sulfide deposit, Québec, Canada. Miner Deposita 30:439–448. https://doi.org/10.1007/BF00196403

Maghfouri S, Mousivand F, Rastad E, Lentz DR (2021) Chemical composition of magnetite and chlorite from the stringer zone of the Nudeh volcanogenic massive sulfide (VMS) deposit, Iran: geological implications. Miner Petrol 115:241–256. https://doi.org/10.1007/s00710-021-00737-z

Maiden KJ, Chimimba LR, Smalley TJ (1986) Cuspate ore-wall rock interfaces, piercement structures and the localization of some sulfide ores in deformed sulfide deposits. Econ Geol 81:1464–1472. https://doi.org/10.2113/gsecongeo.81.6.1464

Mäki T (1986) Lithogeochemistry of the Pyhäsalmi zinc-copper-pyrite deposit, Finland. In: Seventh International Symposium. Institution of Mining and Metallurgy, London, Kuopio, pp 69–82

Mäki T, Puustjärvi H (2003) The Pyhäsalmi massive Zn-Cu-pyrite deposit, Middle Finland—a Paleoproterozoic VMS-class "giant." In: Ashton J et al. (eds), Europe's major base metal deposits. Irish Association for Economic Geology, Dublin, pp 87–91

Mäki T, Imaña M, Kousa J, Luukas J (2015) Chapter 7—the Vihanti-Pyhäsalmi VMS belt. In: Maier WD, Lahtinen R, O'Brien H (eds) Mineral deposits of Finland. Elsevier, pp 507–530

Marshall B, Gilligan LB (1987) An introduction to remobilization: Information from ore-body geometry and experimental considerations. Ore Geol Rev 2:87–131. https://doi.org/10.1016/0169-1368(87)90025-4

Marshall B, Gilligan LB (1989) Durchbewegung structure, piercement cusps, and piercement veins in massive sulfide deposits; formation and interpretation. Econ Geol 84:2311–2319. https://doi.org/10.2113/gsecongeo.84.8.2311

Marshall B, Gilligan LB (1993) Remobilization, syn-tectonic processes and massive sulphide deposits. Ore Geol Rev 8:39–64. https://doi.org/10.1016/0169-1368(93)90027-V

Marshall B, Vokes FM, Larocque ACL (2000) Regional Metamorphic Remobilization: Upgrading and Formation of Ore Deposits. In: Spry PG, Marshall B, Vokes FM (eds) Metamorphic and Metamorphogenic Ore Deposits. Society of Economic Geologists, 19–38

McDonald JA (1970) Some effects of deformation on sulfide-rich layers in lead-zinc ore bodies, Mount Isa, Queensland. Econ Geol 65:273–298. https://doi.org/10.2113/gsecongeo.65.3.273

Meriläinen P (1985) Pyhäsalmen malmista. Dissertation, University of Turku

Miettinen E (2011) Detailed geology of the level - 1275, Pyhäsalmi Mine, central Finland and genetic implications of rock inclusions within the ore body. Dissertation, University of Helsinki

Mookherjee J (1976) Ores and metamorphism: temporal and genetic relationships. Handbook Strata-Bound Stratiform Ore Deposits 4:203–260

Mosier DL, Berger VI, Singer DA (2009) Volcanogenic massive sulfide deposits of the world: Database and grade and tonnage models. US Department of the Interior, Geological Survey Open-File Report

Mustonen A (1998) Kulta Pyhäsalmen malmissa ja sen sivukivissä. Dissertation, University of Turku

Parsons AJ, Ferré EC, Law RD, Lloyd GE, Phillips RJ, Searle MP (2016) Orogen-parallel deformation of the Himalayan midcrust: Insights from structural and magnetic fabric analyses of the Greater Himalayan Sequence, Annapurna-Dhaulagiri Himalaya, central Nepal. Tectonics 35:2515–2537. https://doi.org/10.1002/2016TC004244

Piercey SJ (2010) An overview of petrochemistry in the regional exploration for volcanogenic massive sulphide (VMS) deposits. Geochemistry 10:119–136. https://doi.org/10.1144/1467-7873/09-221

Piercey SJ (2011) The setting, style, and role of magmatism in the formation of volcanogenic massive sulfide deposits. Miner Deposita 46:449–471. https://doi.org/10.1007/s00126-011-0341-z

Plimer IR (1984) The mineralogical history of the Broken Hill Lode, NSW. Aust J Earth Sci 31:379–402. https://doi.org/10.1080/08120098408729300

Putnis A (2002) Mineral replacement reactions: from macroscopic observations to microscopic mechanisms. Mineral Mag 66:689–708. https://doi.org/10.1180/0026461026650056

Putnis A (2009) Mineral replacement reactions. Rev Mineral Geochem 70:87–124. https://doi.org/10.2138/rmg.2009.70.3

Puustjärvi H (1999) Pyhäsalmi modeling project. Outokumpu Mining Oy and Geological Survey of Finland, Technical Report, pp 251

Roberts MD, Oliver NHS, Fairclough MC, Hölttä PS, Lahtinen R (2003) Geochemical and oxygen isotope signature of sea-floor alteration associated with a polydeformed and highly metamorphosed massive sulfide deposit, Ruostesuo, Central Finland. Econ Geol 98:535–556. https://doi.org/10.2113/gsecongeo.98.3.535

Roberts MD, Oliver NHS, Lahtinen R (2004) Geology, lithogeochemistry and paleotectonic setting of the host sequence to the Kangasjärvi Zn-Cu deposit, central Finland: Implications for volcanogenic massive sulphide exploration in the Vihanti-Pyhäsalmi district. Geol Soc Finland Bull 76:31–62. https://doi.org/10.17741/bgsf/76.1-2.003

Rutter EH (1993) Experimental rock deformation: techniques, results and applications to tectonics. Geol Today 9:61–65. https://doi.org/10.1111/j.1365-2451.1993.tb00982.x

Sayab M, Miettinen A, Aerden D, Karell F (2017) Orthogonal switching of AMS axes during type-2 fold interference: insights from integrated X-ray computed tomography, AMS and 3D petrography. J Struct Geol 103:1–16. https://doi.org/10.1016/j.jsg.2017.09.002

Sayab M, Suuronen J-P, Hölttä P, Aerden D, Lahtinen R, Kallonen AP (2015) High-resolution X-ray computed microtomography: a holistic approach to metamorphic fabric analyses. Geology 43:55–58. https://doi.org/10.1130/G36250.1

Timms NE (2003) Garnet porphyroblast timing and behaviour during fold evolution: implications from a 3-D geometric analysis of a hand-sample scale fold in a schist. J Metamorph Geol 21:853–873. https://doi.org/10.1046/j.1525-1314.2003.00487.x

Tomkins AG (2007) Three mechanisms of ore re-mobilisation during amphibolite facies metamorphism at the Montauban Zn–Pb–Au–Ag deposit. Miner Deposita 42:627–637. https://doi.org/10.1007/s00126-007-0131-9

Toulmin P, Barton PB (1964) A thermodynamic study of pyrite and pyrrhotite. Geochim Cosmochim Acta 28:641–671. https://doi.org/10.1016/0016-7037(64)90083-3

Turner FJ (1981) Metamorphic petrology: mineralogical, field, and tectonic aspects, 2d edn. Hemisphere Pub. Corp, McGraw-Hill

Vaasjoki M, Sakko M (1988) The evolution of the Raahe-Ladoga zone in Finland: isotopic constraints. Geol Surv Finland Bull 343:7–32

Vernon RH (2018) A practical guide to rock microstructure. Cambridge University Press, Cambridge. https://doi.org/10.1017/9781108654609

Vokes FM (1969) A review of the metamorphism of sulphide deposits. Earth-Sci Rev 5:99–143. https://doi.org/10.1016/0012-8252(69)90080-4

Vokes FM (2000) Ores and metamorphism: introduction and historical perspectives. Econ Geol Rev 11:1–18

Weihed P, Arndt N, Billström K et al (2005) 8: Precambrian geodynamics and ore formation: the Fennoscandian Shield. Ore Geol Rev 27:273–322. https://doi.org/10.1016/j.oregeorev.2005.07.008

Zhang J, Deng J, Chen HY, Yan LQ, Cooke D, Danyushevsky L, Gong QJ (2014a) LA-ICP-MS trace element analysis of pyrite from the Chang'an gold deposit, Sanjiang region, China: implication for ore-forming process. Gondwana Res 26:557–575. https://doi.org/10.1016/j.gr.2013.11.003

Zhang Y, Sun F, Li B et al (2014b) Ore textures and remobilization mechanisms of the Hongtoushan copper–zinc deposit, Liaoning, China. Ore Geol Rev 57:78–86. https://doi.org/10.1016/j.oregeorev.2013.09.006

Zheng Y, Gu L, Tang X, Wang Z, Wu C, Zhang W, Wu X (2012) Sulfide remobilisation from sulfide ore at high temperatures and differential stresses: an experimental approach. Resour Geol 62:174–186. https://doi.org/10.1111/j.1751-3928.2012.00187.x

Zheng Y, Wang Y, Chen H et al (2016) Micro-textural and fluid inclusion data constraints on metallic remobilization of the Ashele VMS Cu-Zn deposit, Altay, NW China. J Geochem Explor 171:113–123. https://doi.org/10.1016/j.gexplo.2016.06.015

Zhong R, Brugger J, Chen Y, Li W (2015) Contrasting regimes of Cu, Zn and Pb transport in ore-forming hydrothermal fluids. Chem Geol 395:154–164. https://doi.org/10.1016/j.chemgeo.2014.12.008

Zhou F, Gou L, Xu X, Tian Z (2023) Metamorphic ages and PT conditions of amphibolites in the Diebusige and Bayanwulashan complexes of the Alxa Block, North China Craton. Minerals 13:1426. https://doi.org/10.3390/min13111426